Thesis for the Degree of Master in Nanotechnology and Nanoscience

This thesis was conducted under the program
Erasmus Mundus Master: Nanotechnology and Nanoscience, with trajectory
Katholieke Universiteit Leuven (Belgium) - Chalmers University of Technology (Sweden)

Microwave and noise properties of YBCO films and Josephson junctions for quantum circuit applications

Quentin Smets

Supervisors:
Floriana Lombardi & Thilo Bauch

June 2010

Quantum Devise Physics Laboratory
Department of Microtechnology and Nanoscience
Chalmers University of Technology
Göteborg, Sweden 2010

Microwave and noise properties of YBCO films and Josephson junctions for quantum circuit applications
Quentin Smets

Technical report 12L
Department of Microtechnology and Nanoscience
Quantum devise physics Technology

Quantum Devise Physics Laboratory
Chalmers University of Technology
SE-412 96 GÖTEBORG, Sweden
Phone: +32 484667741

Author e-mail: qsmets@gmail.com

Printed by Chalmers Reproservice
Göteborg, 2010

Contents

Motivation of this thesis work

The high-critical temperature superconductivity (HTS) of cuprates has been the subject of intensive research in the last few decades. At the time of this writing, a complete microscopic theory that can fully explain the superconductive properties of HTS is still missing.

It has been established that the order parameter of HTS is mainly of d-wave shape. Therefore it was long assumed that nodal quasi-particles would make it impossible to observe quantum behaviour in HTS. However, recent experiments have shown that HTS Josephson junctions can exhibit macroscopic quantum effects [1, 2]. Indeed, the fabrication of HTS Josephson junctions has been very important to understand the unconventional symmetry of the order parameter. Moreover, Josephson junctions are a fundamental building block for superconducting circuits and offer very interesting quantum applications.

In our research group, we are interested in the intrinsic dissipation in a YBCO Josephson junction using the transmon qubit design. The environmental noise in the transmon design is strongly suppressed. The junction is embedded in a co-planar waveguide resonator structure. The dissipation in the junction is then obtained by measuring the relaxation time of the coupled system (junction and resonator).

The realization of YBCO Josephson junctions with multilayer technology has proven to be a very difficult task. Problems arise due to the very short coherence length of YBCO and the surface instability of the material. Instead, artificial grain boundary junctions fabricated with the biepitaxial technique have shown great flexibility. The grain boundary is obtained by inducing different growth orientations with a patterned seed layer. In this way, junctions can be realized at arbitrary positions on the same chip.

To fulfill the main requirements of the transmon design, the width of the junction must be below 100nm. When the Josephson junction is patterned to these small sizes by ion-beam milling, the YBCO at the edges of the junction suffers extensive damage and the superconductivity is severely degraded due to oxygen outdiffusion. This damage can be prevented by using a new soft nano-patterning approach ("green phase" technique). It combines conventional nanofabrication techniques with principles of self-assembly.

Before realizing a full-YBCO transmon qubit, several tasks need to be fulfilled.

- The grain boundary of the junction must be characterized in detail. The transport of Cooper pairs and quasi-particles through the grain boundary is not very well known, and we need to gain more insight in those mechanisms.

- The other sources of dissipation in the transmon design must be analyzed, in particular the dissipation in the large electrodes of the junction. Determining this is essential to extract the purely intrinsic dissipation of the junction from the relaxation time.

These two tasks are the focus of my thesis work. The first chapter gives a brief introduction on superconductivity, the Josephson effect and the working principle of the transmon qubit. Chapter 2 handles the basic properties of YBCO and the fabrication of YBCO thin films with different crystal orientations. The fabrication of nanosized junctions with the green phase technique is also explained. In chapter 3, the uniformity of the grain boundary and the noise properties of biepitaxial Josephson junctions are measured for different grain boundary angles. The measurements were carried out together with Luca Galletti from Universita' degli studi di Napoli. The high-frequency properties of YBCO will be analyzed in chapter 4. This is done by fabricating YBCO resonators and measuring their quality factor at various temperatures. These measurements give information about the temperature dependence of the London penetration depth and the surface resistance for film grown with different orientations.

This thesis is closely related to the work of several people in our research group:

- Beniamino Iandolo analyzed the properties of biepitaxial YBCO junctions at different angles, made with the new green phase technique [3].
- David Gustafsson is studying the properties of YBCO with a single electron transistor.
- Mudassar Mumtaz Vrik analyzed the high-frequency dissipation properties of MgO substrates with Niobium resonators [4].
- Karin Cedergren studied the influence of the microstructure of the grain boundary in YBCO biepitaxial junctions [5].
- Martin Sandberg realized a transmon qubit embedded in a tunable coplanar waveguide resonator using Aluminum as superconducting material [6].

Keywords: YBCO, d-wave, noise properties, biepitaxial growth, josephson junctions, grain boundary, green phase, pulsed laser deposition, superconducting qubits, transmon, coplanar waveguide, quarter wavelength, quality factor, london penetration depth

Chapter 1

Superconductivity and the Josephson Junction

1.1 Introduction in superconductivity

Superconductivity was discovered by Kamerlingh Onnes in 1911, just after the liquefaction of Helium. The low temperatures allowed him to cool mercury to only a few Kelvin, where he noticed an abrupt drop in the resistivity of the metal. Later, a whole range of metals were discovered to become superconducting when cooled to low enough temperatures. These superconductors are known as low critical-temperature superconductors (LTS), and can be described by the BCS theory [7] developed by Bardeen, Cooper and Shieffer in 1957.

Superconductivity is described by two basic phenomena: perfect conductivity, meaning zero resistance, and perfect diamagnetism. The latter is also called the *Meissner effect*: a magnetic field $B(x)$ decays rapidly with a law

$$B(x) = B_{ext} \exp\Big(-\frac{x}{\lambda_L}\Big) \tag{1.1}$$

where B_{ext} is the external magnetic field and x is measured form the surface of the superconductor. The characteristic decay length λ_L is called the *London penetration depth*. The penetration of the field in the superconductor is shown in figure 1.1.

When a material becomes superconductive, the free electrons condensate into *Cooper pairs*. These are two coupled electrons with opposite momentum and spin. The force responsible for this is a weak attractive force which is mediated by virtual phonons. This interaction with the crystal lattice allows them to flow through the material without collisions. The length over which the electrons remain coupled to each other is called the coherence length ξ.

The Cooper pair is not a fermion but a boson, since the total spin of a Cooper pair is zero. This allows them to collectively occupy the lowest energy level. Their common wavefunction Ψ is called the order parameter . It is described by the Cooper pair density

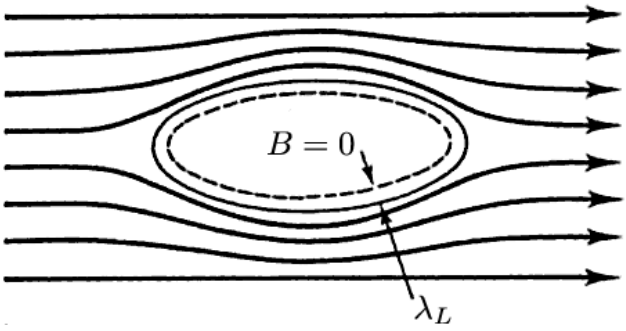

Figure 1.1: Supercurrents screen the magnetic field inside the superconductor. The field penetrates the edges of over a distance λ_L. Figure adapted from [8].

n_P and the phase θ as

$$\Psi(\mathbf{r}) = \sqrt{n_P}\, e^{i\theta(\mathbf{r})} \tag{1.2}$$

The probability density is $|\Psi \cdot \Psi^*| = n_P$. The order parameter of LTS has a s-wave symmetry. This means the amount of energy required to break up the Cooper pair, also called the superconducting gap Δ, is the same in all k-space. This is depicted in figure 1.2.

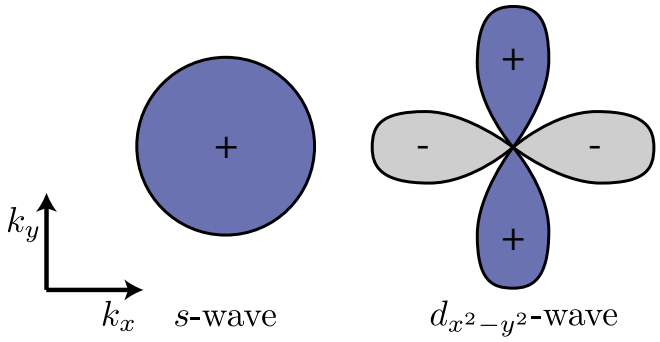

Figure 1.2: The shape of the superconducting gap Δ in $k_x - k_y$-space. LTS superconductors are s-wave, but HTS superconductors are mainly d-wave.

In 1986 there was the discovery of a new class of superconductors by J.G. Bednorz and K.A. Müller: the High-critital temperature superconductors [9]. They have a quite complex structure whose unit cell is a combination of perovskite elementary cells. $YBa_2Cu_30_{7-\delta}$ was one of the first to be discovered. HTS are characterized by a very short coherence length, $\xi \approx 1nm$. The origin of high-temperature superconductivity is not yet understood, but it has been established that the order parameter of HTS has an unconventional type of symmetry and is mainly d-wave [10, 11]. The variation of the energy gap Δ in k-space for a d-wave symmetry is also depicted in figure 1.2, and is

given by

$$\Delta = \Delta_0 \big[\cos(k_x a) - \cos(k_y a) \big] \tag{1.3}$$

For certain angles the superconducting gap becomes zero. The elementary excitations in superconductors are quite different from electrons in a normal metal. They are a combination of electron-like and hole-like excitations (quasi-particles). A comparison of the density of states for quasi particles in LTS and HTS is given in figure 1.3.

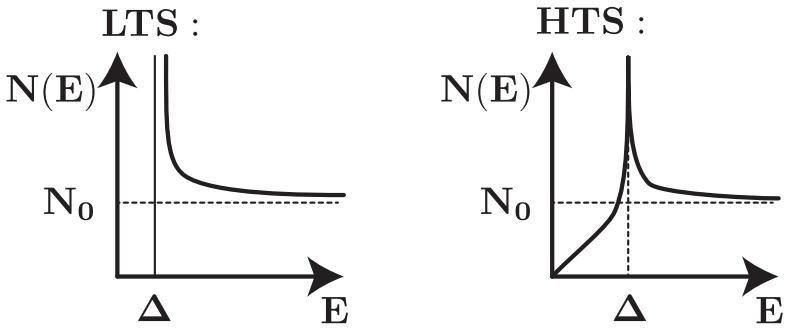

Figure 1.3: The quasi particle density of states for LTS and HTS at zero temperature. LTS have no quasi-particle excitations below Δ, but HTS do have quasi-particles at low energies due to $\Delta = 0$ in certain directions. [12]

1.2 The Josephson effect

1.2.1 The Josephson relations

Let us consider two superconductors separated by a thin insulating barrier, as shown in figure 1.4. A weak link is formed between the superconducting slabs when their order parameters overlap. This type of structure is called a superconducting tunnel junction or Josephson junction. It can be realized with a metal-insulator-metal stack, grain boundaries, very narrow constrictions or damaged regions.

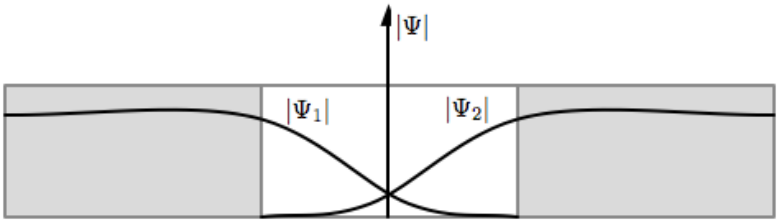

Figure 1.4: A superconducting tunnel junction consisting of a superconductor-insulator-superconductor stack. The order parameters Ψ_1 and Ψ_2 overlap in the insulating region, allowing for tunneling of Cooper pairs through the junction.

In 1962 B.D. Josephson predicted that Cooper pairs could flow through the junction without applying any voltage [13]. This effect was observed two years later by Anderson and Roswell [14]. The behavior of the Josephson junction is given by the following equations

$$I = I_c \sin\varphi \tag{1.4}$$

$$\frac{\partial\varphi(t)}{\partial t} = \frac{2e}{\hbar}V(t) \tag{1.5}$$

$\varphi = \theta_2 - \theta_1$ is the phase difference of the order parameter in the left and right electrodes of the Josephson junction, and I_c is the critical current of the junction which depends on the coupling strength and the Cooper pair densities. The energy gain due to the weak coupling is obtained by integrating the current-voltage product

$$E(t) = \int_0^t I_c \sin\varphi \frac{\hbar}{2e}\frac{\partial\varphi}{\partial t}dt = -\frac{\hbar I_c}{2e}(1-\cos\varphi) \tag{1.6}$$

The prefactor $E_J = (\hbar/2e)I_c$ is called Josephson energy. Using the Josephson equations, one can easily see that the Josephson junction acts as a nonlinear inductor that has the expression

$$L_J = \frac{\hbar}{2eI_c\cos\varphi} \tag{1.7}$$

This strong non-linearity is fundamental for many applications of the Josephson effect. From a circuital point of view a Josephson junction can be seen as a non-linear inductor connected in parallel with a capacitor and a resistor. This is the resistively and capacitively shunted junction (RCSJ model), shown in figure 1.5. The resistive branch

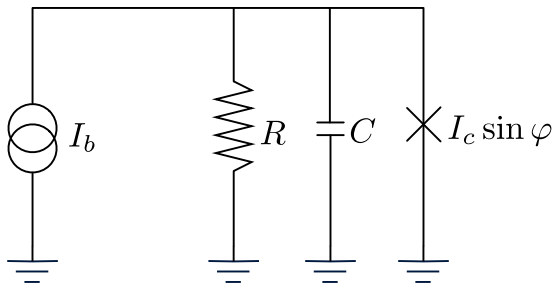

Figure 1.5: Equivalent circuit for the Josephson junction in the RCSJ model

originates from the dissipation due to quasi-particles in the superconductor. The capacitance comes from the dielectric nature of the barrier, and the charging energy is $E_C = e^2/C_J$. Using Kirchoff's law one obtains

$$I_b = \frac{\hbar}{2eR}\frac{d\varphi}{dt} + \frac{\hbar C}{2e}\frac{d^2\varphi}{dt^2} + I_c\sin\varphi \tag{1.8}$$

1.2.2 The washboard potential

Equation (1.8) can be understood through the mechanical analogue of a particle moving in the potential

$$U(\varphi) = -E_J \cos\varphi - \frac{\hbar I_b}{2e}\varphi. \tag{1.9}$$

$U(\varphi)$ is a cosine potential that is tilted by the bias current I_b. Therefore it is often called tilted washboard potential (shown in figure 1.6). The phase of the junction φ maps to the position of the particle. When $I_b < I_c$ the particle is trapped in a local minimum, enable to escape. The junction is in the superconducting state and the voltage over the junction is $V = 0$. When $I_b > I_c$ the phase particle escapes from the minimum. The junction is said to be in the running or voltage state.

If the capacitance C is neglected, the junction is only shunted by the resistor R. This is known as the RSJ model, and the voltage over the junction can be analytically calculated:

$$V = \begin{cases} 0 & \text{for } I_b < I_c \\ \\ I_c\, R\sqrt{(I_b/I_c)^2 - 1} & \text{for } I_b > I_c \end{cases} \tag{1.10}$$

The I-V-curve is shown in figure 1.6.b. The friction of the particle is so high that the inertia can be neglected and the trajectory of the particle is that of the washboard potential. When the bias current is reduced below I_c, the phase particle will be trapped in a new potential well and the superconductive state is recovered.

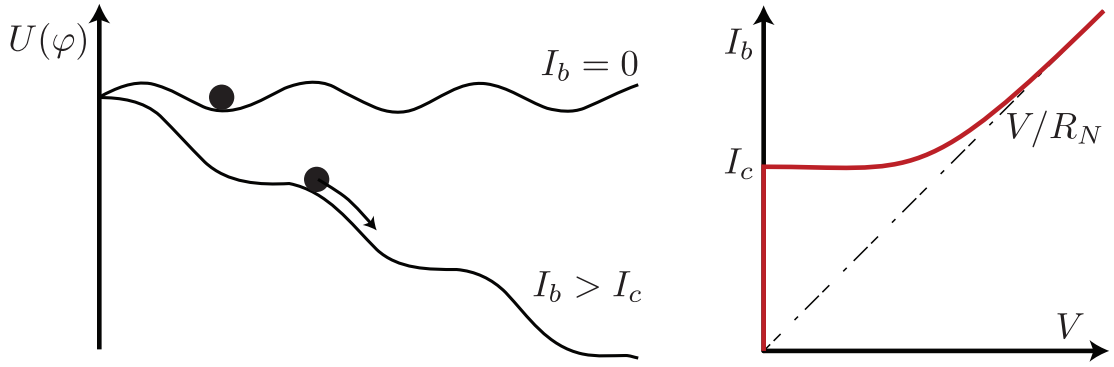

Figure 1.6: a) The Josephson junction can be seen as a phase particle in a tilted washboard potential. When $I_b > I_c$ the junction is in the running state. b) The I-V curve of the Josephson junction in the RSJ model. For high bias currents $I_b \gg I_c$ the transport in the junction is dictated by Ohm's law $V = R\, I_b$

If the capacitance is too large to be neglected, equation (1.8) cannot be solved analytically. However one can understand the behavior of the junction through the mechanical analogue. When the bias current is increased to $I_b > I_c$, the phase particle escapes the minimum and switches abruptly to the running state. When the bias current is decreased

again below I_c, the inertia of the particle will prevent it from returning immediately to a local minimum. It will only return to the superconductive state if I_b is decreased so that the particle hits the top of the following well (figure 1.7). The value of this bias current is the retrapping current I_r, which can be significantly lower than I_c.

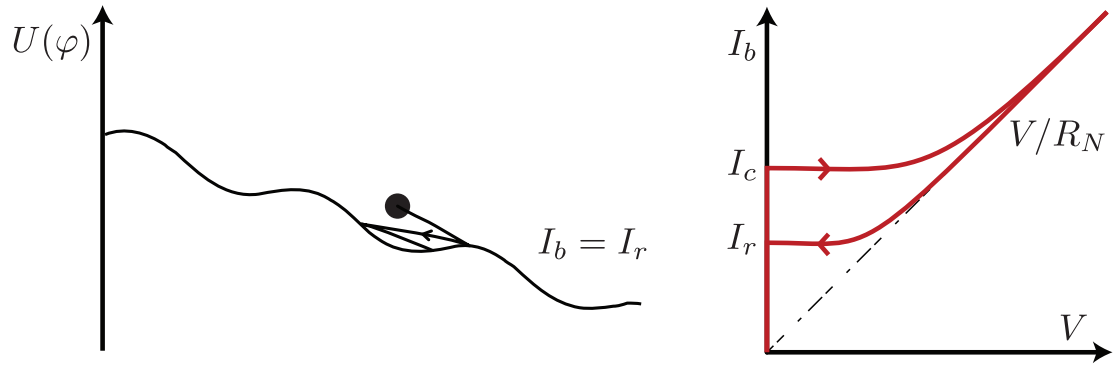

Figure 1.7: The superconducting state is only recovered if the phase particle hits the top of a potential bump. Therefore a significantly lower I_b must be applied and the I-V curve is hysteretic.

1.2.3 The Josephson junction in a magnetic field

Similarly to superconductors, a Josephson junction screens external and self-induced magnetic fields from it's interior by inducing supercurrents. The field decays with a characteristic length λ_J from the surface of the junction. λ_J is the Josephson penetration depth and is given by

$$\lambda_J = \sqrt{\frac{\Phi_0}{2\pi\mu_0 d_{\text{eff}} J_c}}. \tag{1.11}$$

$\Phi_0 \equiv h/2e$ is the flux quantum. $d_{\text{eff}} = d + 2\lambda_L$ is the effective thickness of the junction. λ_J determines the magnetic length of the junction. If $W < \lambda_J$, the field penetrates the junction in a uniform way. The junction is said to be magnetically short. If $W > \lambda_J$, the penetration will be non-uniform and the junction is magnetically long.

Consider the case where a Josephson junction is placed in an externally applied magnetic field $\mathbf{H}$, oriented as in figure 1.8. The penetration of the field will lead to a variation of the phase difference $\varphi(x)$ along the x-direction according to the relation

$$\nabla\phi = \frac{2e}{\hbar} d_{\text{eff}}(\mathbf{n} \times \mathbf{B}). \tag{1.12}$$

For a magnetically short, rectangular junction with a uniform current density $J_c(x, y) = J_c$, one can easily obtain [15] that the critical current can be expressed as a function of the magnetic flux $\Phi = B\, d_{\text{eff}} L$:

$$I_c(B) = I_c(0)\left|\frac{sin(\pi\Phi/\Phi_0)}{\pi\Phi/\Phi_0}\right| \tag{1.13}$$

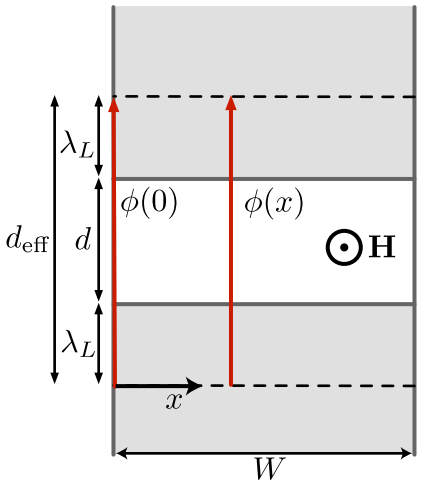

Figure 1.8: When the junction is placed in an external magnetic field, the phase difference ϕ is dependent on the position x

Here $I_c(0) = AJ_c$ is the critical current without any applied field and A is the cross-section of the junction. The variation of the critical current is shown in figure 1.9 and resembles the diffraction pattern through a narrow slit. For this reason it is often referred to as a Fraunhofer pattern. A measurement of this pattern can be a useful

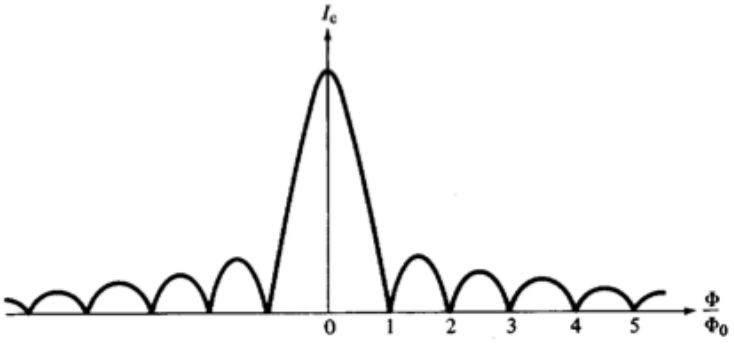

Figure 1.9: The Fraunhofer pattern shows the variation of I_c with the applied flux.

way to determine the uniformity of the critical current in the junction. HTS Josephson junctions often result in a distorted Fraunhofer pattern due to the non-uniformity of the barrier. This is further discussed in chapter 3.

1.3 The transmon design

1.3.1 Superconducting qubits

In order to gain a better understanding in the mechanisms leading to high-temperature superconductivity, it is important to study the intrinsic properties of HTS Josephson junctions. Quite recently, Koch et al. have considered a Josephson junction in a coplanar waveguide [16], the transmon. With their design one can extract information about the intrinsic source of dissipation in a Josephson junction since the system is strongly decoupled from the environment. In what follows we shall briefly review the working principle of Koch's design which also represents one of the most promising two-level quantum systems (qubits).

Superconducting qubits are solid state artificial two-level systems based on the Josephson effect. The energy levels of the circuit potential are quantized, and only the two lowest levels $|0\rangle$ and $|1\rangle$ are selected for the operation of the qubit. The transition to higher energy levels is prevented by the non-linearity of the Josephson junction. This makes the circuit potential anharmonic and different energies are needed for the transition to other levels $E_{0\to1} \neq E_{1\to2} \neq E_{2\to3} \ldots$. This is shown in figure 1.10.

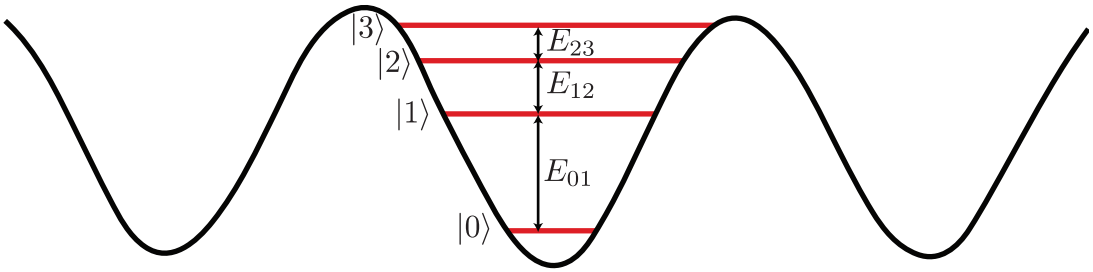

Figure 1.10: The operation can be restricted to the levels $|0\rangle$ and $|1\rangle$ because the circuit potential is anharmonic. The transition energies to higher levels are all different.

The qubit operation must be performed in a timespan shorter than the coherence time: the amount of time before the qubit coherence is lost. This can be either because of random switching between the energy levels (relaxation) or by a randomization of the qubit phase (dephasing). Maintaining the qubit in a coherent state is not an easy task; the circuit must be decoupled from the environment to prevent unwanted state transitions, but at the same time a certain level of coupling is required to perform read and write operations. Due to this delicate balance the coherence time of superconducting qubits is on the order of a few μs, but a lot of progress is being made in the field [17].

Superconducting qubits are divided into 3 main classes, according to their relevant degree of freedom (figure 1.11): the phase qubit [18], the flux qubit [19] and the charge qubit [20–22]. It should be noted that the qubits are not described using microscopic degrees of freedom, but rather using collective electrodynamical modes of macroscopical electrical elements [17]. The main difference between the qubits is the ratio of Josephson

energy and charging energy of the Josephson junction, E_J/E_C.

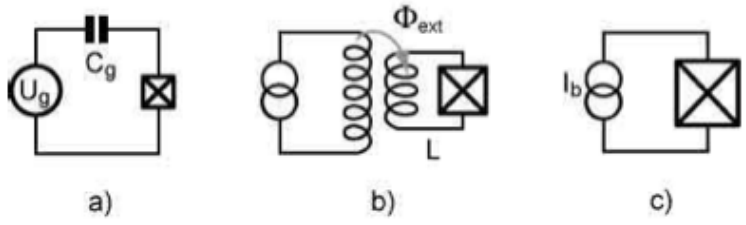

Figure 1.11: The basic types of superconducting qubits: a) the charge qubit, b) the flux qubit and c) the phase qubit [17]

The phase qubit has the largest E_J/E_C ratio and operates in the phase regime. It is a current biased Josephson junction, and the circuit potential is the tilted washboard potential. The first and second states of the anharmonic circuit potential are used as qubit states, and the energy splitting between the two states $E_{01} = \hbar\omega_a$ is tuned with the bias current.

The flux qubit uses the orientation of the flux through the loop as qubit states. It is tuned by coupling the circuit to an external flux Φ_{ext}.

The charge qubit consists of a superconducting island which is capacitively coupled to a gate. The states are defined by the tunneling of a single Cooper pair to this island. Therefore it is called a Single Cooper pair box. For a more in-depth review on superconducting qubits, we suggest the following reviews: [17, 23].

1.3.2 Types of noise in qubits

Superconducting qubits are affected by 3 types of noise: charge noise, flux noise and critical current noise. A high amount of noise will destroy the coherence of the qubit, through either energy relaxation or dephasing. The main problem of the charge qubit is the high sensitivity to low-frequency 1/f charge noise. This leads to a short phase coherence time.

The short phase coherence can be improved in 2 ways: The first approach is to reduce the noise itself through careful selection of the right materials [24], thinking from a material science point of view. The second approach is to improve the design of the qubit and decrease the sensitivity to noise.

1.3.3 The transmon qubit

The transmon qubit was introduced by Jens Koch in 2007 [16]. The basic structure is based on a Josephson junction embedded in a co-planar waveguide. The Josephson junction operates in the regime where the ratio of Josephson energy and charging energy is $E_J/E_C \sim 50$. This gives an exponential suppression of the sensitivity to $1/f$ charge

noise. The charge dispersion is virtually eliminated, and as a result the dephasing times are dramatically improved.

The circuit implementation of the transmon is depicted in 1.12. The Josephson junction has no DC connections to the rest of the circuit and it is biased with zero current. It can be replaced by a loop of two Josephson junctions (dc-SQUID setup) to allow the tuning of the Josephson energy $E_J = E_{J,max}|cos(\pi\Phi/\Phi_0)|$ by changing the applied magnetic flux Φ through the loop. The regime $E_J/E_C \sim 50$ is reached by shunting the Josephson junctions by a large capacitor C_B. The charging energy is $E_C = e^2/2C_\Sigma$ with $C_\Sigma = C_J + C_B + C_g$.

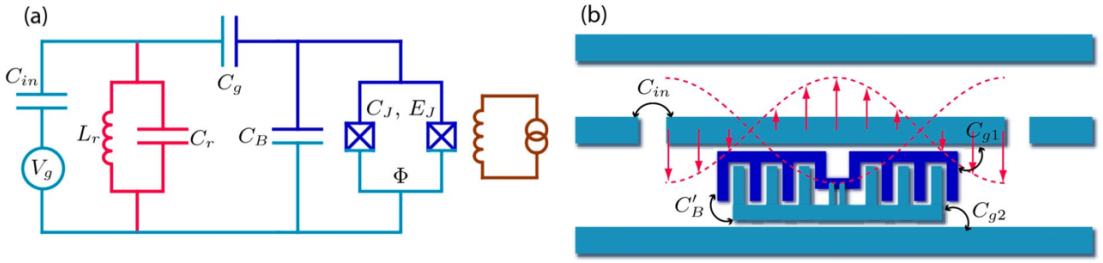

Figure 1.12: a) The equivalent circuit of the transmon qubit. b) The transmon consists of a SQUID placed in a coplanar waveguide. The ratio E_J/E_C is obtained with the large shunting capacitor C_B. [16]

The energy levels of the transmon are calculated by visualizing it as a single Cooper pair box where the gate offset charge is n_g. The effective qubit Hamiltonian is found by solving the stationary Schrödinger equation[1] in the phase basis $\hat{\phi}$:

$$\hat{H} = 4E_C(\hat{n} - n_g)^2 - E_J\, cos(\hat{\varphi}). \tag{1.14}$$

The lowest three eigenenergies E_1,E_2 and E_3 are plotted in figure 1.13 as a function of the gate charge offset n_g. One can see that an increase in $E_J \gg E_C$ results in an exponential decrease in charge dispersion $\partial E_{01}/\partial n_g$. At a ratio around $E_J/E_C \sim 50$ the qubit becomes virtually insensitive to $1/f$ charge noise. The energy splitting E_{01} is equal to the plasma frequency of the Josephson junction with zero current bias. On the other hand, large values of $E_J \gg E_C$ also decrease the level of anharmonicity $(E_{21} - E_{01})/E_{01}$. This makes qubit operations more difficult, as a sufficiently large anharmonicity is needed to prevent excitations to higher energy levels in the system. However is has been shown [16] that this decrease in anharmonicity is algebraic, but the decrease in charge dispersion is exponential (with parameter $\sqrt{8E_J/E_C}$). With this setup the dephasing time is increased [26] to values up to $3\mu s$. This makes the transmon qubit a very viable superconducting qubit.

The transmon design is interesting because the Josephson junction is embedded in a co-planar waveguide (CPW) resonator[2]. The resonance frequency of the resonator

[1] The full derivation with circuit quantization is available in [16, 25]

[2] The CPW resonator is discussed in more detail in chapter 4

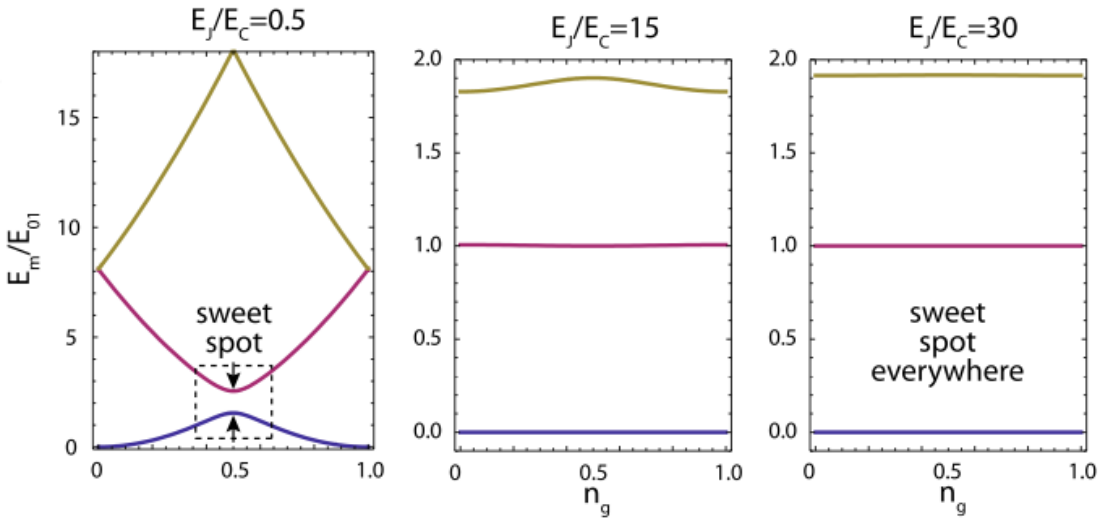

Figure 1.13: The first three eigenenergies of the transmon as a function of the gate offset n_g for different ratios E_J/E_C. The energies are normalized to the transition energy E_{01} at the degeneracy point $n_g = 1/2$. When $E_J/E_C \sim 50$ the qubit is insensitive the charge noise [26]

is shifted depending on the state of qubit. This makes the readout of the qubit state possible. Write operations are performed by injecting photons with microwave frequency in the resonator. When the energy of the photon is equal to the level splitting (the plasma frequency of the Josephson junction) they can trigger a state transition.

The resonator shields the Josephson junction from the environment by only allowing certain microwave frequencies in the cavity. This is the reason why we want to use the transmon qubit design. The measurement of the dephasing time allows us to probe the intrinsic properties of the YBCO Josephson junction by isolating it from other noise sources.

This thesis is not about the realization of a complete YBCO transmon qubit. Instead we focus on tackling a few specific problems. First YBCO Josephson junctions need to be realized which meet the required ratio of $E_J/E_C \sim 50$ (chapter 2). Once they can be fabricated in a reproducible way, the main source of decoherence [27] is investigated, which is the critical current noise of the junction (chapter 3). Another source of decoherence is the quasi-particle dissipation in the large YBCO electrodes of the capacitor C_B. Therefore, the microwave dissipation properties are investigated by fabricating YBCO resonators and measuring their quality factor (chapter 4).

Chapter 2

Towards nanosized YBCO biepitaxial Josephson junctions

2.1 The crystal structure and superconducting properties of YBCO

The superconductivity of $YBa_2Cu_30_{7-\delta}$ (YBCO) was established by Wu et al. in 1987 [28]. This discovery was revolutionary, since the critical temperature of the superconductor was well above liquid nitrogen temperature ($T_c = 93K$). Like other high-temperature superconductors, YBCO is characterized by a perovskite crystal structure. It is composed of CuO_2 layers separated by Barium and Copper atoms. The crystal structure of is shown in figure 2.1.

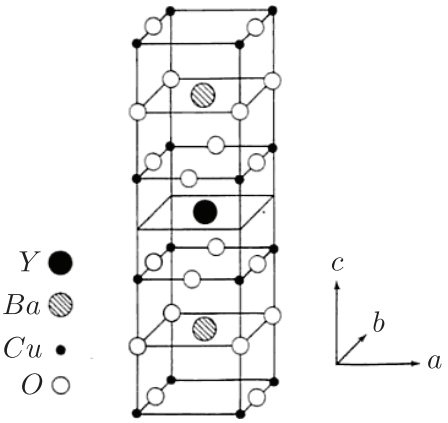

Figure 2.1: YBCO has a perovskite crystal structure. It consists of Cu-O planes separated by alternating Yttrium and Barium atoms. adapted from [29]

Like other HTS, YBCO is characterized by a range of interesting properties which make them much more complex than low-temperature superconductors. The source

of superconductivity is believed to be the presence of mobile charge carriers in the CuO_2-planes. This is also the reason why the properties of YBCO are so anisotropic. The superconductive properties in the $\hat{c}$-axis direction are much weaker than in the (ab)-planes, giving rise to a very anisotropic length scales. For instance in the (ab)-plane, λ_{ab} is around $130nm$, but in the $\hat{c}$-axis direction λ_c can reach a few μm. These numbers are highly dependent on the oxygen doping of the crystal. The phase diagram is shown in figure 2.2. In addition, the Cooper pair coherence length is extremely short in comparison with LTS: ξ_{YBCO} is on the order of $1.5nm$ in the (ab)-plane. This makes it very sensitive to variations in impurity concentration and grain boundaries. Although these properties pose a challenge for the reproducible fabrication of YBCO circuits, it is the most extensively studied high-temperature superconductor.

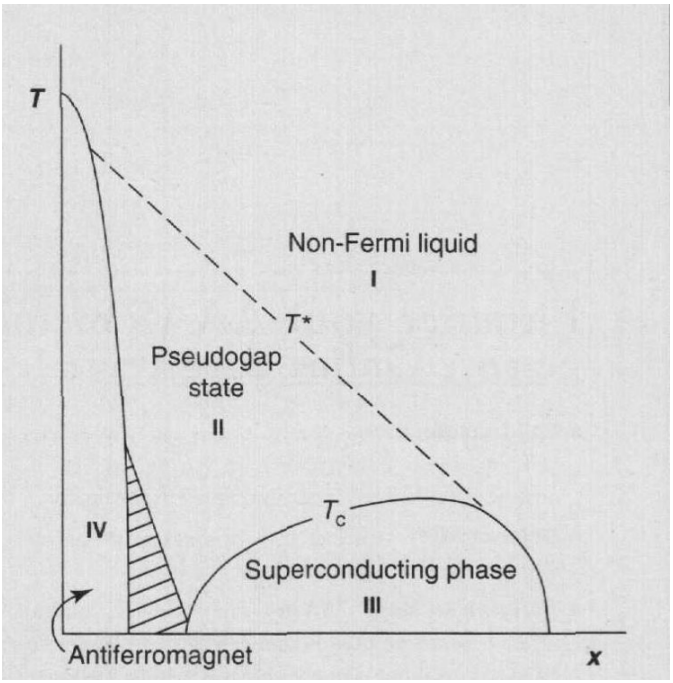

Figure 2.2: YBCO is superconducting for a certain range of oxygen doping. [30]

2.2 Biepitaxial Josephson junctions

Conventionally, LTS Josephson junctions are made using the so-called trilayer configuration: a stack of superconductor-insulator-superconductor (SIS) material is subsequently deposited. Cooper pairs must then tunnel through the insulator material, giving rise to the Josephson effect. Since LTS have a long coherence length ($\xi_{Al} \sim 1600nm$), they are quite insensitive to small defects and variations in the microstructure of the junction. It is difficult to implement the SIS structure for HTS Josephson junctions. Since they

have an extremely short coherence length both in the (ab)-plane and in the $\hat{c}$-axis direction, the properties of the junctions are be very sensitive to random changes in the microstructure.

It turns out that a grain boundary in the HTS thin film can be effectively used to make a Josephson junction. The region between grains with a different crystallographic orientation can have a weakened superconductivity, leading to the Josephson effect in certain conditions [31].

There are a number of ways to make an artificial grain boundary in a superconducting thin film, among them there are the bicrystal [32] and the biepitaxial [33] techniques. The bicrystal technique makes use of two monocrystals of different orientation which are glued together. This usually gives high-quality junctions, but it is impossible to place the junctions at arbitrary positions on the chip. The biepitaxial method solves this problem by inducing different growth orientations with a seed layer. The HTS thin film will have grain boundaries that follow the pattern of the seed layer. The seed layer must be thin enough, because the patterning will create a step directly underneath the biepitaxial junction. The epitaxial growth on this step is much more complicated and makes the junctions less reproducible.

Depending on the angle of the seed layer edge, the grains will meet at different orientations and the properties of the junction will be different. This can be used to tune the properties of the junction.

2.3 Epitaxial growth of YBCO thin films

All samples were fabricated in the MC2 Nanofabrication laboratory[1] of the Chalmers University of Technology. The growth modes of YBCO have been investigated with X-Ray diffractometry (XRD), Scanning electron microscopy (SEM) and Atomic force microscopy (AFM). Those techniques are introduced in appendix A.

2.3.1 Substrate and seed layer selection

The biepitaxial technique allows us to grow various grain boundaries, depending on the substrate and the seed layer used. The substrates where the thin films are deposited need to have a good match with the crystal lattice of the YBCO. In the group, previous research has been conducted to MgO and CeO_2 seed layers on (110) $SrTiO_3$ substrates [5]. In this thesis, 5x5mm (110) MgO substrates are used instead, as they have a dielectric constant $\epsilon = 9.65$ instead of $\epsilon = 277$ for $SrTiO_3$ [34]. The very high ϵ of $SrTiO_3$ substrates induces an additional stray capacitance in parallel with the grain boundary, which affects the properties of the junctions. Moreover, $SrTiO_3$ is not suitable for high frequency measurements. The substrates have a 6° vicinal cut in the $[1\bar{1}0]$ in-plane direction. The vicinal cut will be further discussed in section 2.3.5. $SrTiO_3$ was chosen as a seed layer material to induce a different orientation of YBCO with respect to the MgO substrate.

[1] http://www.chalmers.se/mc2/EN/laboratories/nanofabrication

2.3.2 Pulsed laser deposition of YBCO thin films

PLD has proven to be a very effective method for depositing YBCO films [35]. Because all the elements are ablated simultaneously, the stoichiometry is conserved. More conventional techniques like physical vapor deposition (sputtering) or evaporation have been less successful.

The $SrTiO_3$ and YBCO films are deposited on the substrates with the Pulsed Laser Deposition (PDL) TWIN system. The machine is custom built at Chalmers and capable of depositing multiple materials without breaking vacuum, and also of in situ ion beam milling. A picture of the chamber and the setup of the machine are shown in figure 2.3.

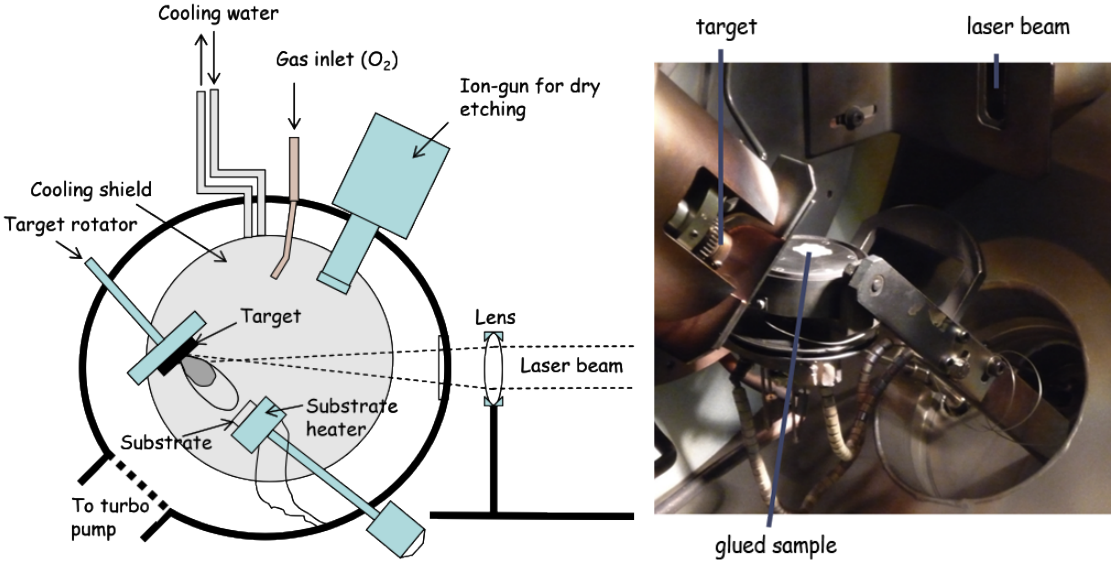

Figure 2.3: The PLD *TWIN* system from the MC2 clean room

A high-energy laser pulse is fired on the rotating target. This causes an explosive non-equilibrium evaporation of the target material in a narrow plume. This happens in a low-pressure oxygen environment. The material is deposited on the sample which is glued on a heater. The time between the pulses must be high enough to allow the atoms to rearrange for the epitaxial growth.

During the pulsed laser deposition, several parameters need to be carefully tuned to obtain smooth epitaxial films. The full recipe is given found in appendix D.

Energy of the laser pulse When the laser pulse hits the target, the material explodes very locally and is directed towards the sample in a plume of plasma. The stoichiometry of the plume is only conserved if the delivered energy is correct. Moreover, the energy density over the area of the laser pulse must be uniform. This is done by cutting off the

edges of the pulse with an aperture. The energy density was calibrated to 1.8 J/cm^2 for one pulse, and the pulse frequency is 1Hz for STO and 10Hz for YBCO.

The substrate temperature and frequency of the laser pulses The substrate temperature needs to be high enough to allow the atoms to position themselves correctly during the epitaxial growth. Moreover the frequency of the pulses should be low enough to give the atoms enough time to diffuse to the right position. $SrTiO_3$ was deposited at 720°and YBCO was deposited at various temperatures ranging from 770°C to 820°C.

The O_2 pressure in the deposition chamber The presence of oxygen in the chamber is necessary to dope the YBCO thin film with a sufficient amount of oxygen atoms. Moreover, the shape of this plume is controlled by the pressure in the chamber. The oxygen content was typically 0.2 mbar during the STO deposition and 0.4 to 0.6 mbar during the YBCO deposition

2.3.3 Growth of YBCO on MgO substrates

YBCO grows in the [001]-orientation on the (110) MgO substrate.The $\hat{c}$-axis is aligned normal to the crystal structure of the MgO. Samples have been fabricated by pulsed laser deposition under different conditions. The parameters for the different samples are given in appendix D.1. The crystal structure of these samples was analyzed with a 2θ-ω XRD scan[2], and the result is shown in figure 2.4. There is constructive interference on the (00n) planes of the YBCO, and the orientation is indeed (001). The in-plane rotation of several films has been measured by a Φ-scan. Figure 2.4.b shows a film without rotation (the red curve has very sharp peaks only for the $\Phi = n\,\pi/2$ angles) and a film with mixed rotation (the green curve has peaks at $\Phi = n\,\pi/2$ and $\Phi = n\,\pi/2 + \pi/4$). These results are not reproducible and it is not yet understood what influences the in-plane rotation of (001) YBCO.

2.3.4 Growth of $SrTiO_3$ seed layers on MgO substrates

30nm $SrTiO_3$ seed layers have been deposited by pulsed laser deposition. The films grow with a (110) orientation on (110) MgO. This was inspected by XRD, and the results are shown in figure 2.5. There is a very large peak for the MgO substrate at 62.3° and a peak for the thin (110)-oriented STO layer at 32.4°.

2.3.5 Growth of YBCO on $SrTiO_3$ seed layers

When YBCO is deposited on the $SrTiO_3$ seed layer, it can grow either in a [103] orientation or a $[\bar{1}03]$ orientation, (see figure 2.6). This is due the 180°in-plane symmetry of the $SrTiO_3$ (110) seed layer. When the grains of different orientation meet, intrinsic tilt grain boundaries are formed in the thin film. A solution to this problem is to use a substrate with a vicinal cut. The grains where the $\hat{c}$-axis is closer to the normal will

[2]XRD is discussed in appendix A.

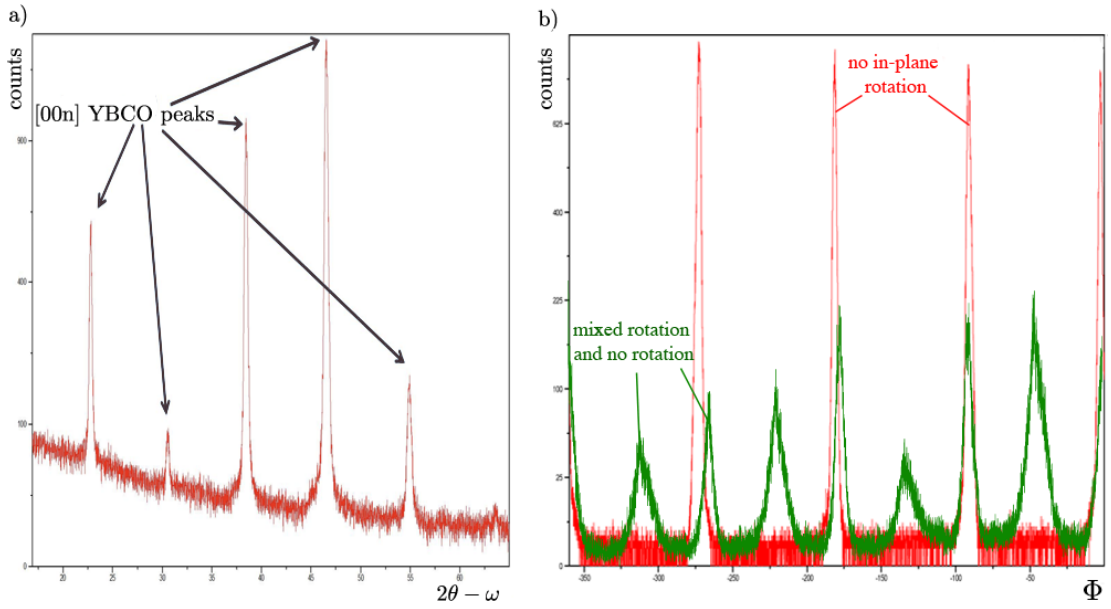

Figure 2.4: a)2θ-ω scan of (001) YBCO film. b)Φ-scan of (001) YBCO films with in-situ ion beam milling. The parameters of the films with green and red signals are $T_{dep} = 790°$and $p_{dep} = 0.6$ mbar

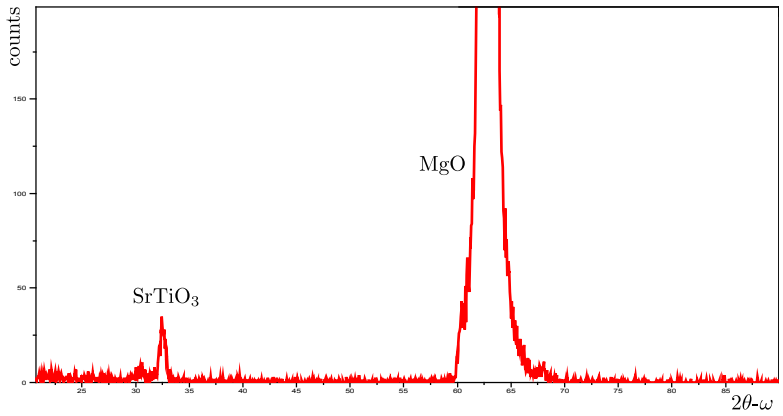

Figure 2.5: 2θ-ω scan of a [110]-oriented STO seed layer on an MgO substrate. The deposition parameters for $SrTiO_3$ are $T_{dep} = 700°$C and $p_{dep} = 0.2$ mbar

grow faster. Therefore all the grains are forced in the [103]-orientation (figure 2.7). The film has a granular structure due to the different growth speed in the (ab)-plane and the $\hat{c}$-axis direction. It has been found that lower substrate temperatures lead to a merging of the grains, which decreases the surface resistance R_s of the thin film. Picture 2.8 shows how the (103) grains are merged when the YBCO is deposited at 770° C.

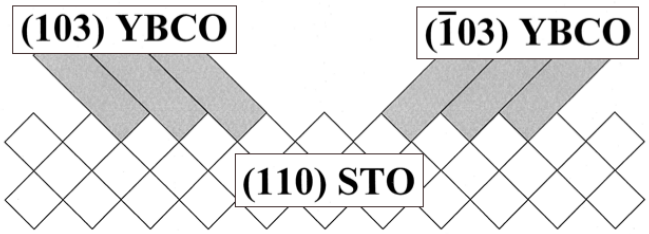

Figure 2.6: (103) YBCO can grow in two different orientations on the $SrTiO_3$. adapted from [36]

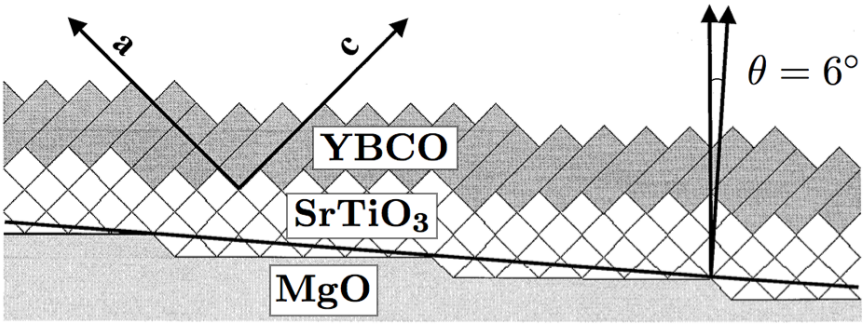

Figure 2.7: If substrates with a 6° vicinal cut are used, the (103) YBCO grains are forced in the same orientation. adapted from [36]

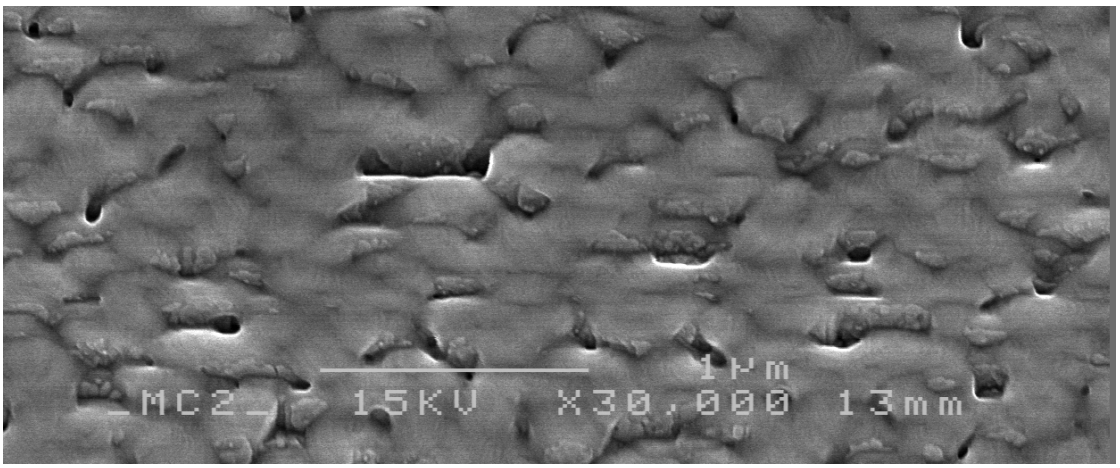

Figure 2.8: The granular structure of (103) YBCO is merged. The deposition parameters for this film are $T_{dep} = 770°C$ and $p_{dep} = 0.6$ mbar

In this thesis the fabrication of a pure (103) film has proven to be the most difficult part. This is because the competition between the (001) and (103) growth modes is

very sensitive to the morphology of the seed layer. In total, sixteen samples have been fabricated in order to obtain a pure (103)YBCO film. Unfortunately, most of them were a combination of (001)and (103)YBCO. A SEM image of one of those samples is shown in figure 2.9a., and the darker regions are (001) YBCO. Figure 2.9.b shows the XRD mapping of the same sample. The left peak at 32.8° shows that the film is mainly

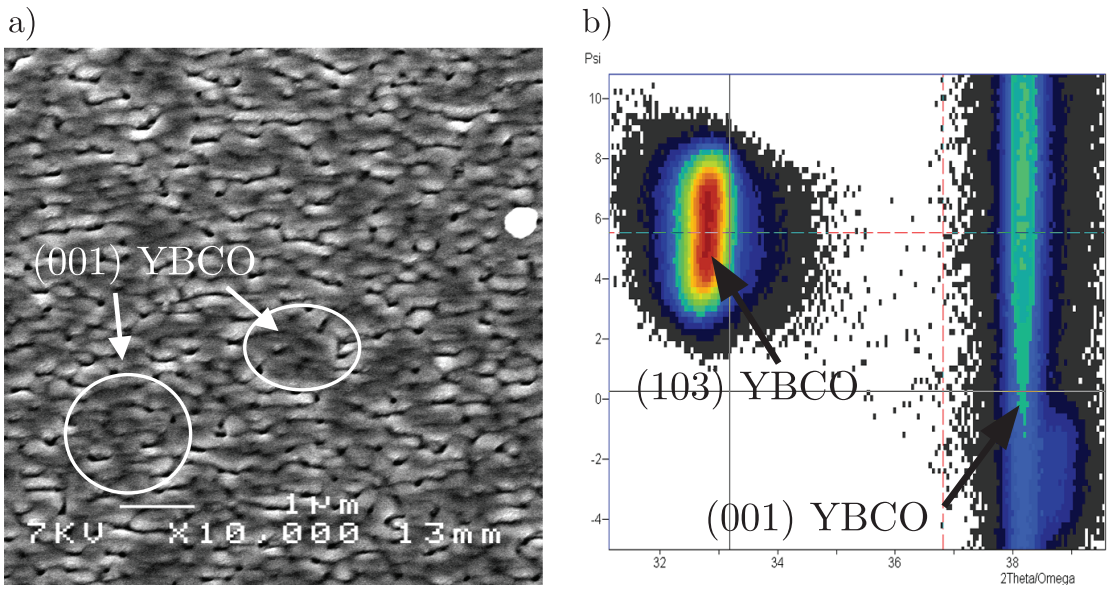

Figure 2.9: a) parameters: T_{dep} = 790°C and p_{dep}=0.6 mbar. The darker, merged spots are regions of (001) YBCO. b) This is confirmed by a Ψ-mapping.

(103) orientated, but the right peak at 38.8° indicates a strong presence of (001) YBCO. Moreover, the peak is stretched out in the Ψ direction, meaning the (001) grains are spread over different Ψ orientations, and the film is polycrystalline.

However, we managed to grow a fully (103)-orientated film. The Φ-mapping of this film shows there is only a very low percentage of (001) YBCO (figure 2.10.b). The microstructure was investigated by AFM (figure 2.10.a), and the image shows the typical granular structure. The dissipative properties of these films were analyzed by patterning them in co-planar waveguide resonator geometry. This is discussed in chapter 4.

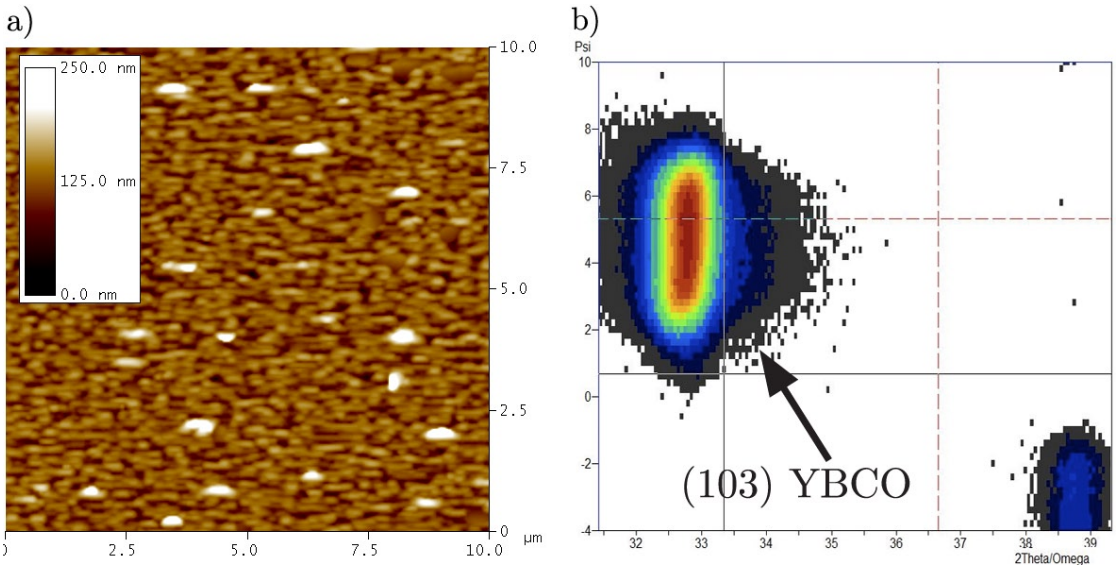

Figure 2.10: a) The AFM picture shows the granular structure of the (103) film. The deposition parameters are $T_{dep} = 800°C$ and $p_{dep} = 0.6$ mbar. (AFM picture taken with scan rate = 0.2 Hz, tapping mode, 256x256 samples) b) The Ψ-mapping of this sample shows there is only a very low concentration of (001) YBCO.

2.4 YBCO Biepitaxial Josephson Junctions

YBCO biepitaxial junctions are obtained with the following procedure

- Pulsed laser deposition of $SrTiO_3$ seed layer on the MgO substrate
- Patterning of the seed layer with e-beam and ion-beam milling
- Pulsed laser deposition of YBCO on the seed layer and the bare substrate
- Patterning of the YBCO junction with ion beam milling

As the orientation of the seed layer edge is changed, different grain boundaries are defined (2.11). The grain boundary is a result of a crystal rotation along different crystal axes. Between points C-D the grain boundary is of the type [100]-45° tilt + [001]-45° tilt. We define this orientation as the 0° angle. Between points A-B the grain boundary is [100]-45° twist + [001]-45° tilt. We define this orientation as the 90° angle. At intermediary angles the grain boundary is a mix of these two rotations. The transport properties along the different grain boundaries are quite different, since the lobes of the d-wave order parameter overlap in different ways. For 0° junctions the transport is partly in the $\hat{c}$-axis direction, but in 90° junctions the transport happens fully in the (ab)-planes of the YBCO. The patterning of the seed layer thus allows us to realize Josephson junctions with a whole range of different transport properties.

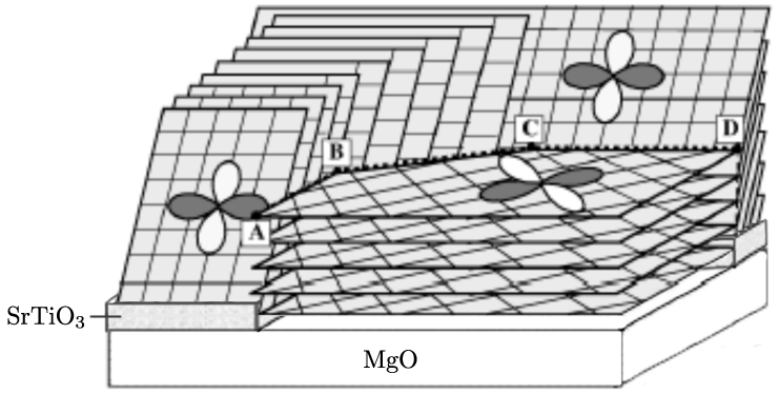

Figure 2.11: The overlap of the d-wave order parameter is different as the angle of the seed layer is changed. By patterning the seed layer in different ways, junctions with different transport properties are realized

2.5 A new approach to nanosized YBCO Josephson junctions with green phase

A transmon qubit requires a ratio of Josephson energy over charging energy of $E_J/E_C \sim 50$. $E_J = I_c\Phi_0/2\pi$ is defined by the critical current of the junction, and experiments in chapter 3 show that YBCO biepitaxial junctions have a critical current density on the order of $J_c = 30\mu A/\mu m^2$. The charging energy is $E_C = e^2/2C_j$ with C_j the capacitance of the junction. Previous studies have shown that the capacitance per unit area is around $C_j/A = 260fF/\mu m^2$ [37]. If the fim thickness is around 120nm, the transmon regime is reached for a junction width $W \sim 100nm$. It is very hard to reach these junction widths by conventional Ar-ion beam milling since the edges of the YBCO junction are heavily damaged. This destroys the superconductivity of YBCO. In nanosized junctions, the damaged portion is quite significant, and junctions smaller than 100nm cannot be fabricated in this way [38].

When a YBCO film grows epitaxially, a number of secondary phases with different stoichiometry are formed, depending on the deposition conditions. In case of (001) YBCO on (110) MgO substrates, precipitates of Y_2BaCuO_5 (Y211) form when the deposition temperature is lowered to 750°C. This so-called green phase is insulating. A SEM picture of this green phase is shown in figure 2.12. The dissipation properties of films with a high amount of green phase are also a subject of investigation in chapter 4.

Nanometer size junctions can be created by combining the self-assembly of green phase with conventional fabrication techniques. According to Scotti di Uccio et al., the green phase nucleates preferentially at grain boundaries [39]. After the growth of the biepitaxial junction, the interface is analyzed with SEM and AFM to find small connections enclosed by insulating green phase (figure 2.13). The Josephson junction is defined by this single connection, which is then isolated with Focused ion beam (FIB).

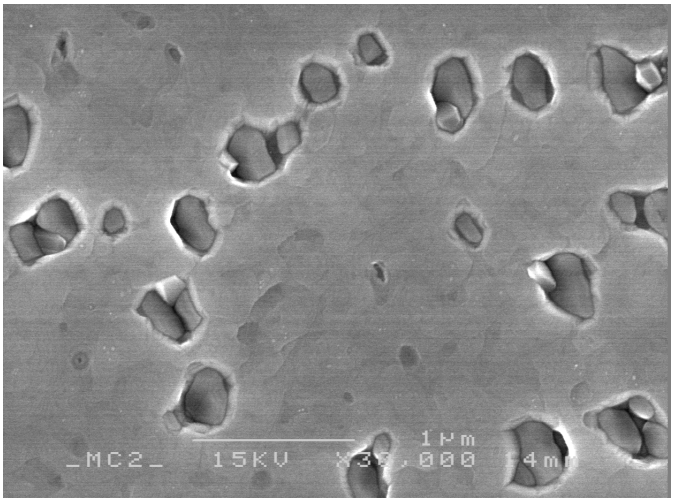

Figure 2.12: (001) YBCO with a high concentration of green phase. $T_{dep} = 790°C$ and $p_{dep} = 0.6$

The YBCO is milled at a distance of 300-400nm away from the junction, which prevents the junction from being damaged by ion-implantation. With this technique it is possible to obtain junction sizes of less than 100nm.

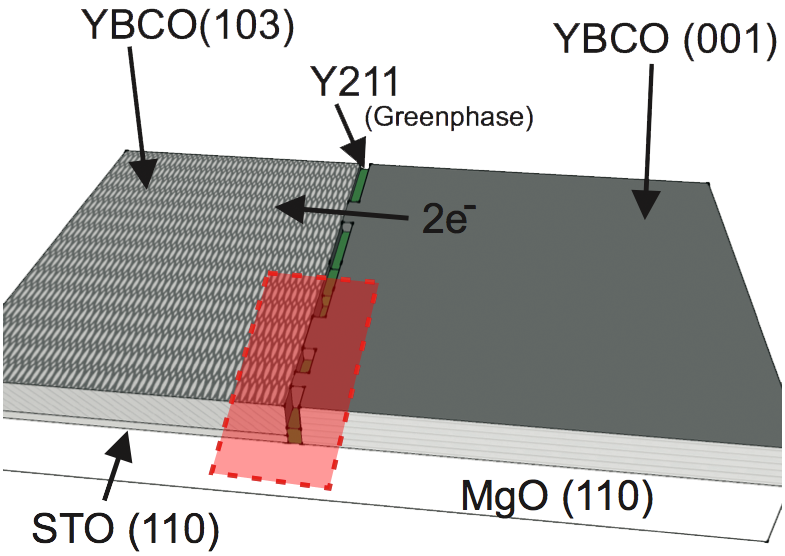

Figure 2.13: The junction is constricted by the green phase on the grain boundary. After the connection is located with AFM and SEM, the red parts are milled away with FIB. adapted from [3]

Chapter 3

Noise measurements on YBCO biepitaxial Josephson junctions

3.1 Types of noise in biepitaxial grain boundaries

In this chapter, we report on the noise properties of biepitaxial YBCO Josephson junctions. Noise measurements are a helpful tool to study the transport mechanisms across the grain boundary: the critical current noise $S_I = |\delta I_c/I_c|^2$ and normal resistance noise $S_R = |\delta R_N/R_N|^2$ give information about the cooper pair and quasi-particle transport respectively. Fluctuations in critical current are the main source of dephasing in the transmon qubit; The Josephson energy is directly dependent on the critical current $E_J = (\hbar/2e)I_c$, and these variations lead to a changing qubit level splitting during the measurement and hence to dephasing of the qubit [27].

The low-frequency critical current noise S_I and resistive noise S_R are due to charge trapping states in the barrier. These are metastable states that can momentarily trap quasi-particles [24, 40, 41]. This trapping causes a decrease in the effective area of the junction due to Coulomb repulsion (lower transparency). The lower effective area decreases the critical current and increases the normal resistance. One individual charge trap causes a random telegraph switching of I_c and R_N with a Lorentzian spectrum. When the grain boundary contains many charge traps the spectra are convoluted to a $1/f$ noise spectrum [42].

The amount of relative fluctuations in critical current noise and normal resistance noise give information about the uniformity of the junction. This ratio q is defined by

$$q \equiv \frac{S_I}{S_R} \tag{3.1}$$

When the transport in the junction is homogenous (both in the x-direction along the grain boundary and in the current transport direction), one can assume that the product of I_c and R_N is constant: $I_c R_N \sim \Delta$ with Δ the energy gap of the superconducting material [8]. Therefore, $q = 1$ for a homogenous barrier and the fluctuations of critical current and normal resistance are anti-correllated $\delta I_c/I_c = -\delta R_N/R_N$.

HTS Josephson junctions usually follow the Intrinsic Shunted Junction model (ISJ) where the barrier assumed to be inhomogeneous [43]. It contains a high number of localized states, where the quasi-particle transport is higher due to resonant tunneling. In this case, the product I_cR_N is not constant. Instead it depends on the critical current density accorging to $I_cR_N \sim (j_c)^p$. Under these conditions it can be shown that

$$q = \frac{S_I}{S_R} = \frac{1}{1-p} \tag{3.2}$$

The fluctuations in critical current are larger than the fluctuations in normal resistance and one typically obtains a ratio of $q \sim 4$.

Miklich et al. [44] proposed a model for the total voltage noise in HTS Josephson junctions. The voltage noise can be modeled according to the following equation

$$S_v(f) = \left(\frac{\delta V(f)}{V}\right)^2 = (V - R_dI)^2 S_I(f) + V^2 S_R(f) + k(V - R_dI)V S_{IR}(f) \tag{3.3}$$

V is the voltage over the junction written as $V = I_cR_N v(\frac{I}{I_c})$, I is the current through the junction, $R_d = \partial V/\partial I$ is the differential resistance, $S_I = |\delta I_c/I_c|^2$, $S_R = |\delta R_N/R_N|^2$, and $S_{IR} = |\delta I_c/I_c||\delta R_N/R_N|$. The correlation k=-2 for perfect antiphase correlation, k=0 for perfect uncorrelation between S_I and S_R. If the IV-curve has a shape like in the RSJ model, one can see from equation (3.3) that S_I dominates at small bias currents where the differential resistance is high. S_R dominates at high bias currents when the junction is in the resistive regime and S_{IR} only has an influence in the intermediary regime. When the voltage noise is measured at different bias currents, we can used expression (3.3) to extract values for S_I and S_R.

In our group, David Gustafsson measured this ratio for YBCO biepitaxial junctions fabricated with the green phase technique. It was shown that the transport was tunnel-like and and $q \approx 1$ in certain conditions. These junctions could not be modeled by the ISJ model[1]. The aim of this chapter is to further investigate whether YBCO biepitaxial junctions can show LTS-like properties by measuring the ratio q.

3.2 Fabrication of YBCO biepitaxial junctions

Due to the difficulties encountered in growing high-quality (103) YBCO grown on a MgO substrate with a $SrTiO_3$ seed layer, it was not possible to make green phase biepitaxial junctions with this configuration. Instead, the noise was measured on YBCO junctions fabricated on a $SrTiO_3$ substrate with a patterned CeO_2 seed layer. Here the situation is reversed: YBCO grows [103]-orientated on the $SrTiO_3$ substrate and [001]-orientated on the seed layer. The microstructure of the grain boundaries with different orientations does not differ much from those fabricated with MgO as substrate and $SrTiO_3$ as seed layer.

[1]These results have not yet been published, and are therefore not further discussed here.

The fabrication of the sample was done by Karin Cedergren and Luca Galletti. The thickness of the YBCO thin film was much lower than for the films fabricated in chapter 2. For 0°junctions, the epitaxial growth is in such a way that the (*ab*)-planes of (001) YBCO meets only one (*ab*)-plane of (103) YBCO and a basal plane grain boundary is obtained (figure 3.1). After a certain thickness some waviness appears in the grain boundary. By reducing the thickness of the YBCO to 50nm, a purely basal plane junction can be obtained when the grain boundary angle is low ([100]-45° tilt + [001]-45° tilt grain boundary). The CeO_2 seed layer and the junctions are patterned

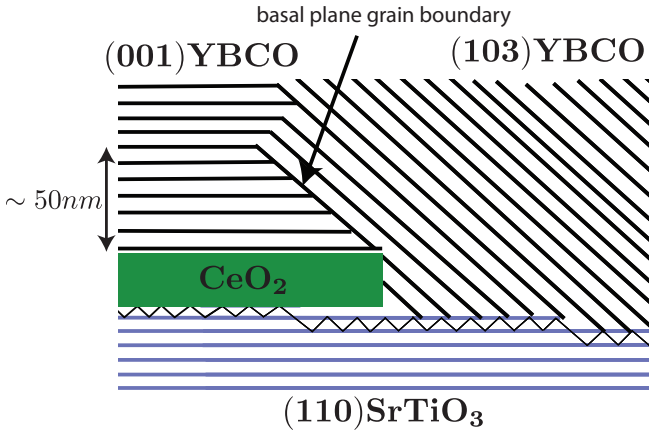

Figure 3.1: The grain boundary grows in a basal plane configuration up to a certain height. Afterwards the (*ab*)-planes meet in a random way. We have chosen to grow thin YBCO films to obtain only one type of grain boundary with a very regular microstructure. adapted from [5].

with a hard carbon mask and Ar^+-ion beam milling. Junctions with different transport properties are obtained by patterning the seed layer as discussed in section 2.4. The sample contains junctions with seventeen different grain boundary angles. For each angle there are four junctions: two junctions with a width of $4.2\mu m$ two of $2.2\mu m$. In total, the chip contains 68 junctions. Figure 3.2 shows an optical picture of the junctions ranging from 0° to 25°.

3.3 Measurement setup

The different junctions are connected to a sample holder with gold wire bonds, with two connections per pad to allow a four-point probe measurement. The sample is cooled using a *HelioxVL Cryostat* from Oxford Instruments. The working principle of the HelioxVL is explained in appendix A.4. A superconducting coil (with a field to current ratio $L = 100mT/A$) is placed around the sample to measure the response of the junctions under a magnetic field. The active junction is chosen by connecting it to a the measuring equipment with a switching board. It is current biased by a *Agylent* 33220A 20MHz waveform generator, and the voltage is extracted by the four-point probe measurement.

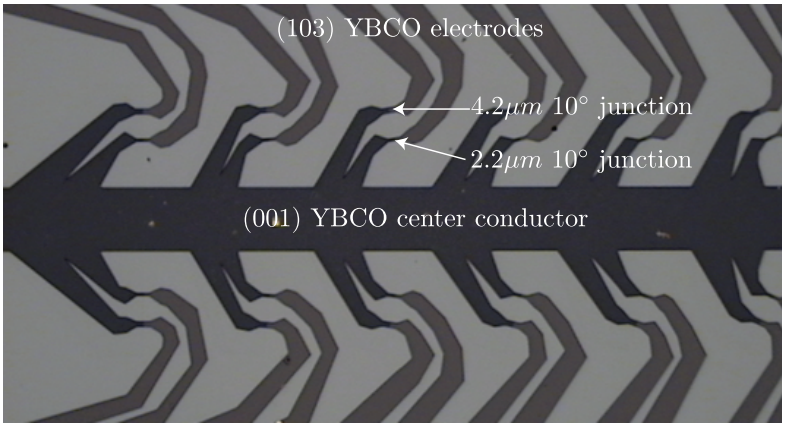

Figure 3.2: An optical picture of the low-angle junctions. The junction is located in the constriction, where (001) YBCO (black) and (103) YBCO (grey) meet. For each angle there are four junctions: two with a width of 4.2 μm and two with a width of 2.2 μm.

The voltage signal is amplified with a *SR560* and measured with a Dynamic Signal analyzer *SR785* from Stanford Research. The data is then fed to the workstation with a GPIB connection.

We measured the magnetic pattern of the junctions. A magnetic pattern is given by the conductance as a function of bias current and magnetic field. This allows us to visualize the change in critical current with the magnetic flux. A magnetic pattern reveals information about the uniformity of the grain boundary ($j_c(x)$). A homogenous grain boundary has a Fraunhofer pattern. More complicated patterns arise when the grain boundary is interrupted by holes or islands of insulating phase.

Despite the fact that the sample is protected by the magnetic shield of the liquid helium dewar, and the whole setup is placed in a shielded room (faraday cage), a lot of measurement problems originated from Abrikosov vortex trapping. The vortices can only be removed by heating the sample above the critical temperature of YBCO ($\sim$ 90K). When a vortex is trapped near the grain boundary, the critical current is changed due to the magnetic field lines crossing the junction.

3.4 Magnetic patterns and AFM measurements

In general, the patterns showed that the junctions were generally quite non-uniform. From the 38 junctions that were measured, none had a conventional Fraunhofer pattern. Instead most junctions showed π-SQUID-like [5] patterns or more complicated patterns due to more than two superconducting channels. Figure 3.3.a shows the pattern of a junction with 70°orientation and 4.2 μm width. The pattern is quite complicated with different superposed modulations, indicating multiple superconducting channels. Figure 3.3.b is a junction with 5°orientation and 2.2 μm width. It is a good example of a π-SQUID, formed by two superconducting channels with opposite current orientations.

When there is no applied magnetic field the critical current approaches zero.

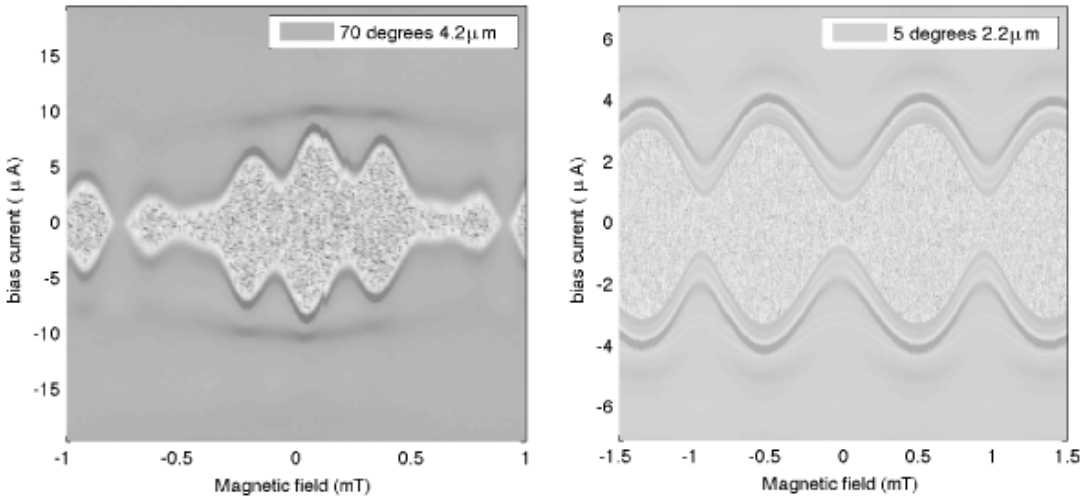

Figure 3.3: The pattern is the junction conductance (greyscale) as function of bias current and magnetic field. a) junction with 70° orientation and 4.2 μm width: it shows a complicated pattern with multiple modulations. b) junction with 5° orientation and 2.2 μm width: π-SQUID-like pattern

In order to obtain absolute values for the critical current density j_c and the normal resistance R_N, the superconducting cross-section of the junction must be known. When the magnetic patterns are Fraunhofer-like, the effective width of a channel can be calculated from the period of the modulations [45]. In our case the patterns were too complicated to make this estimation, so atomic force microscopy (AFM) was used instead. Figure 3.4 shows the 3D plots for the two junctions discussed above. These measurements clearly show the presence of holes at the grain boundary. These holes are responsible for the interference-like magnetic patterns. Possibly the holes are due to the very thin YBCO films (50nm) used in the experiment. Moreover, the seed layer thickness (24nm) is comparable to the YBCO film thickness, inducing a significant step at the grain boundary. In certain situations, where the nucleation centers are far away from the seed layer, the step could prevent the grains from making contact with each-other (figure 3.5). A hole is then created in the grain boundary.

3.5 Noise measurements

We observed from the IV-curves that the junctions had a large amount of hysteresis. This is due to the very high dielectric constant of the $SrTiO_3$ substrate, which causes a large stray capacitance over the grain boundary[2]. Since the junction must be biased at

[2]When the capacitance cannot be neglected (RCSJ model), the retrapping current is much lower than the critical current and the junction is hysteretic.

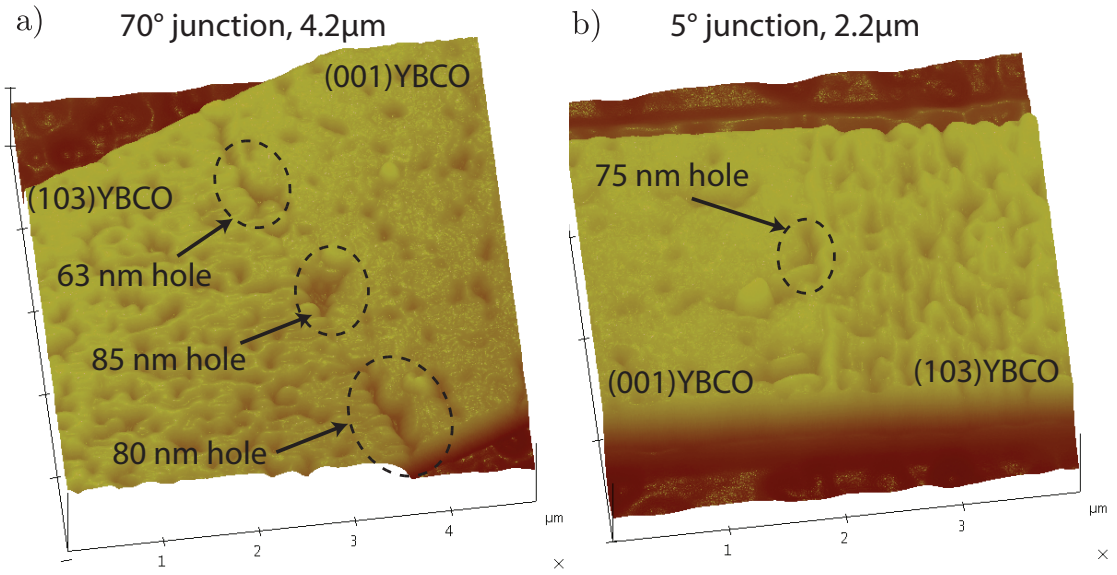

Figure 3.4: a) 70°junction with 4.2 μm width. b) 5°with 2.2 μm width. The junctions show a number of holes at the grain boundary. The data scale of the image (highest to lowest point) is 500nm

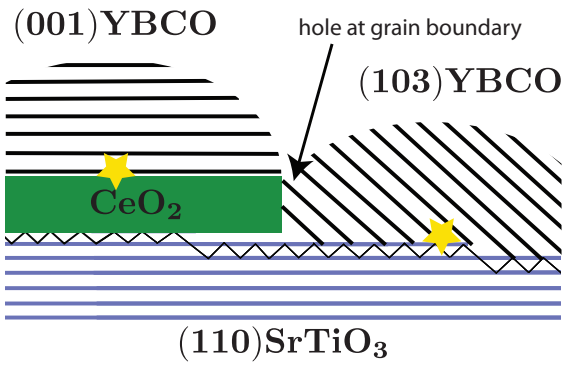

Figure 3.5: It is possible that the grains cannot make a connection when the nucleation center is far away from the grain boundary. The nucleation centers are indicated by yellow stars.

a very specific point of the IV-curve, the noise was measured at temperatures around $40K$ where the hysteresis was supressed. Furthermore, the magnetic field was chosen so that the junction had the highest critical current, or $\partial I_c/\partial\Phi = 0$. This minimizes the flux noise, where random changes in magnetic field $\delta\Phi$ lead to variations in critical current δI_c.

The noise was measured on the two junctions mentioned above, and a junction with 5° orientation and 4.2 μm width. The data points were fitted with equation (3.3). The

results are shown in figure 3.6.

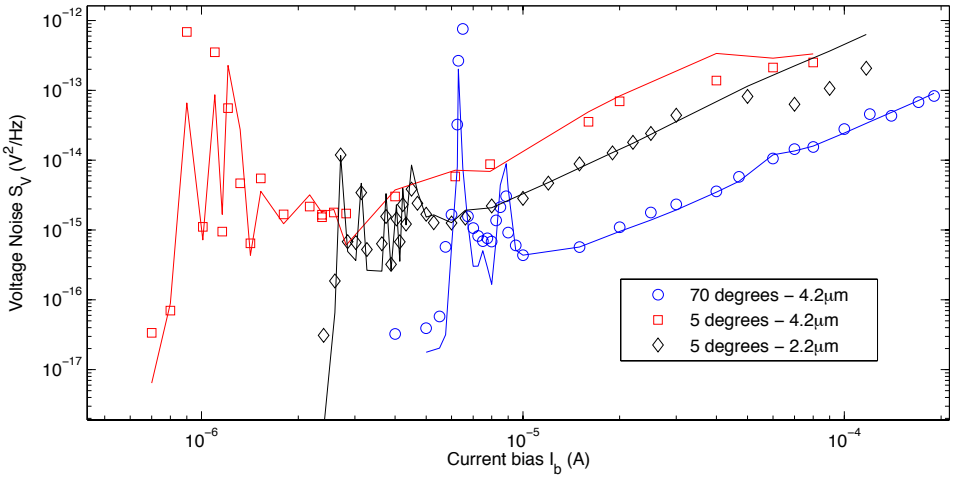

Figure 3.6: The noise S_V as a function of bias current I_B. The noise from the blue pattern was taken at 49K to minimize hysteresis. The red curve was taken at 24K and the black curve at 15K.

The sharp noise peak observed for all three junctions is due to the high differential resistance when the junction switches to the resistive state. The noise is lower for intermediate values and goes up again due to normal resistance noise. The values obtained during the fitting procedure are given in table 3.1.

	S_I (Hz^{-1})	S_R (Hz^{-1})	k	q
junction 70°- 4.2μm	10^{-8}	$1.3 \cdot 10^{-9}$	0	7.7
junction 5°- 4.2μm	$1.5 \cdot 10^{-7}$	$4 \cdot 10^{-9}$	-1.5	37.5
junction 5°- 2.2μm	$2 \cdot 10^{-8}$	$4 \cdot 10^{-9}$	0	5

Table 3.1: The fitted parameters for the noise measurements. $S_I = |\delta I_c/I_c|^2$, $S_R = |\delta R_N/R_N|^2$, k is the correlation parameter and $q = S_I/S_R$

The junction with 5° orientation and 4.2μm width had a very high amount of relative critical current noise. This could be due to regions of normal conductivity in the grain boundary, where there is no cooper pair transport but only quasi-particle transport. This effectively reduces the grain boundary area where supercurrents can flow, and the critical current noise is increased since $S_I \sim 1/A$ with A the superconductive junction area [41].

The value of $q = 1$ for grain boundaries with lower angles could not be confirmed with these experiments. In future work, the width of low-angle junctions will be reduced with focused ion beam to keep only a single superconducting channel. The insulating

and normal conducting parts are then removed. An example of this procedure is shown in figure 3.7. This way, the critical current noise is reduced and lower values of q might be observed again.

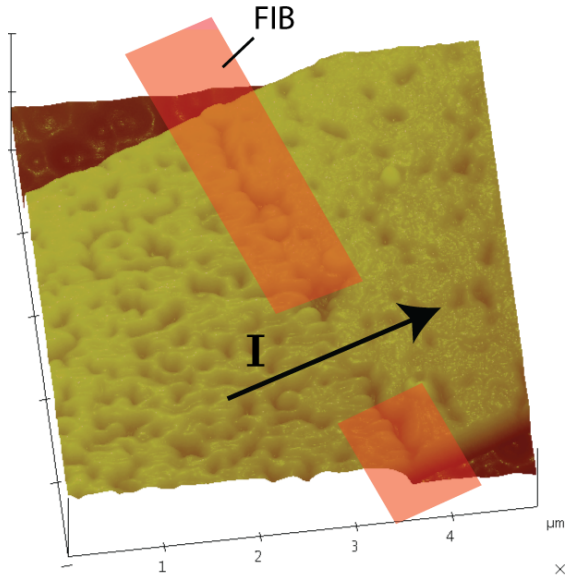

Figure 3.7: The width of the junction is reduced with focused ion beam (red area), so only one superconducting channel remains.

Chapter 4

High-frequency dissipation properties of YBCO

In this chapter, the high-frequency dissipation properties of $YBa_2Cu_30_{7-\delta}$ thin-films on MgO substrates are investigated. The large electrodes of the Josephson junctions consist of (103) YBCO and (001) YBCO. Therefore the dissipation properties of both thin films is investigated. This is realized by fabricating YBCO quarter wavelength resonators, and measure their so-called intrinsic quality factor Q_{int}. Mudassar Mumtaz Vrik measured Q_{int} for Niobium resonators on MgO substrates [4]. It was established that the dielectric losses due to MgO substrates give a quality factor of $Q_{int} = 8000$. If Q_{int} of the YBCO resonators is around the same value, one can conclude that the dissipation is mainly due to the dielectric losses in the MgO substrate. These experiments will also give information about the temperature dependence of the London penetration depth, and the surface resistance R_s of the thin films.

In addition, the quality factor was also measured in the low-power regime. The thin film always contains a certain number of two-level fluctuators. These are defects, impurities and other irregularities that typically lie on surfaces and interfaces. They can be excited by absorbing a photon. When the number of photons injected in the resonator is close to the amount of two-level fluctuators in the superconducting material, a degradation in the quality factor should be observed.

Three different resonators have been fabricated:

- Resonator 1: a (001) YBCO resonator with a higher green phase concentration. It is fabricated by using a YBCO target with a 5% higher Yttrium concentration than the standard $YBa_2Cu_30_{7-\delta}$ stoichiometry.The (Y211) insulating green phase should give rise to a higher surface resistance.
- Resonator 2: a (001) YBCO resonator with a lower green phase concentration. It is fabricated with a target with a 5% lower Yttrium concentration to reduce the nucleation of green phase.
- Resonator 3: a (103) YBCO resonator. The different growth orientation is obtained with a $SrTiO_3$ seed layer.

4.1 The co-planar waveguide resonator

An electromagnetic resonator consists of an inductor L and a capacitor C, either in series or in parallel. It can store energy in the magnetic field of the inductor and the electric field of the capacitor, and the energy oscillates between the two elements. The oscillation frequency is the resonance frequency ω_r[1] and is given by

$$\omega_r = \frac{1}{\sqrt{LC}} \tag{4.1}$$

When the resonator circuit is driven by a signal with frequency ω_i, the energy of the probing signal is absorbed only if ω_i is near the resonance frequency of the resonator ω_r. The resonance peak is obtained by measuring the reflection on the resonator Γ at various frequencies ω_i. The quality of the resonator is determined by the amount of dissipation, and is given by the quality factor Q defined by

$$Q = \frac{\text{Energy stored}}{\text{Energy dissipated per radian}} \tag{4.2}$$

Only a very narrow range of frequencies is absorbed when the dissipation is low. Under certain conditions, the quality factor can be determined from a reflection measurement with the formula

$$Q = \frac{\omega_r}{\text{FWHM}} \tag{4.3}$$

The Full-Width Half-Maximum of the peak (FWHM) is as defined in figure 4.1. The derivation of this relation is given in appendix B.

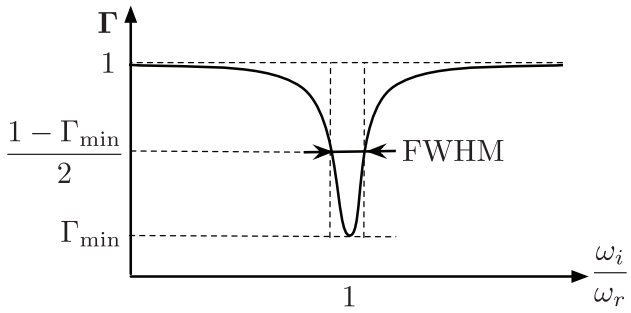

Figure 4.1: Q can be calculated by taking the full-width half-maximum of the resonance peak.

So far, the exact implementation of the resonator has been left open. In this thesis a quarter-wavelength co-planar waveguide is used. A co-planar waveguide (CPW) consists of a center conductor placed on a dielectric substrate. Ground planes are located at each side of the center conductor (figure 4.2). This setup allows for electromagnetic waves (photons) to travel along the CPW. The co-planar waveguide becomes a quarter

[1] A different notation for the frequency is $f_r = \omega/2\pi$. The angular frequency ω is used instead

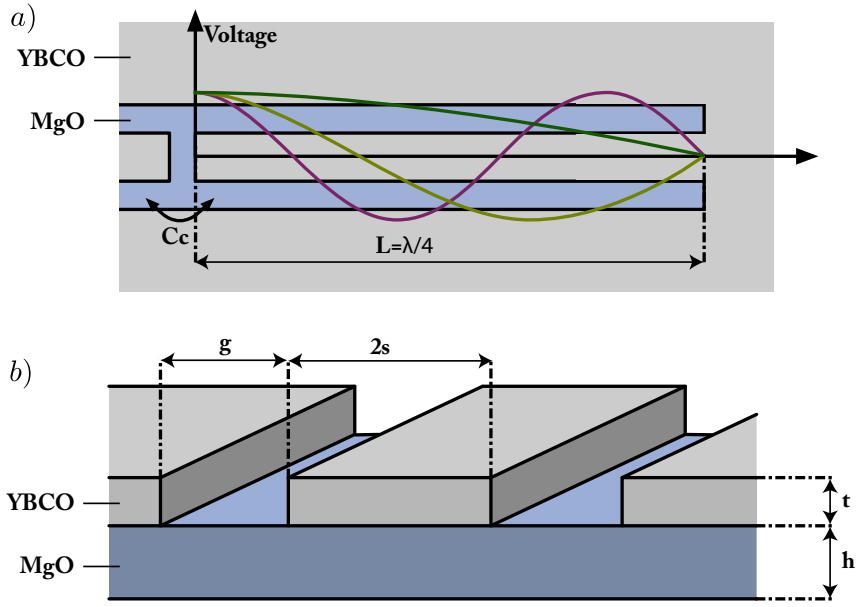

Figure 4.2: a) top view of the quarter wavelength co-planar waveguide resonator. The first three resonance modes are shown. b) Cross section of the YBCO co-planar waveguide on MgO substrate

wavelength resonator when one end is connected to ground (shorted) and the other end is left open. These boundary conditions only allow the electromagnetic modes with a wavelength $\lambda = 4l/(2m+1)$, with l the resonator length and m an integer. These standing waves are depicted on figure 4.2.a. The resonator is driven through a coupling capacitance C_c. The photons will resonate inside the trench for an average time $1/\kappa$ before being absorbed. The decay rate of the photons κ can be defined by

$$\kappa = \frac{\omega_r}{2\pi Q} \tag{4.4}$$

The use of a co-planar waveguide to probe the properties of the material has several advantages.

- The fabrication is easy and does not require any deposition of insulators. Only one mask is needed.
- The design of the co-planar waveguide can be chosen to have a characteristic impedance of 50Ω and match other elements in the circuit.

According to formula (4.2), the quality factor Q is determined by dissipation of energy in the resonator. The quality factor is inversely proportional to the losses, which can be internal and external. The internal losses are due to the intrinsic properties of the

conductor material and the dielectric losses in the substrate and the conductor-dielectric interface. The external losses are due to the coupling of the resonator with the outside world through the coupling capacitance C_c. Since the losses are additive, the quality factor can be split into the external quality factor Q_{ext} and the internal quality factor Q_{int}.

$$\frac{1}{Q} = \frac{1}{Q_{int}} + \frac{1}{Q_{ext}} \tag{4.5}$$

When $Q_{int} > Q_{ext}$ the losses in the resonator are mainly due to the coupling with the outside world, and the resonator is said to be overcoupled. On the other hand, when $Q_{int} < Q_{ext}$ the losses are mainly internal, and the resonator is undercoupled. When $Q_{int} = Q_{ext}$ the resonator is critically coupled.

Close to the resonance frequency the quarter-wavelength CPW resonator can be represented by the lumped element circuit on figure 4.3, the values for Q_{int} and Q_{ext} are

$$Q_{int} = \frac{\omega_r R_{in} C_r [(\omega_r C_c R_g)^2 + 1 + C_c/C_r]}{(\omega_r C_c R_g)^2 + 1} \tag{4.6}$$

$$Q_{ext} = \frac{[1 + (\omega_r C_c R_g)^2] C_r + C_c}{\omega_r C_c^2 R_g} \tag{4.7}$$

Typically one can make the assumption $\omega_r C_c R_g \ll 1$, and the equations reduce to

$$Q_{int} \simeq \omega_r R_{in} (C_r + C_c) \tag{4.8}$$

$$Q_{ext} \simeq \frac{C_r + C_c}{\omega_r C_c^2 R_g} \tag{4.9}$$

Furthermore, if one uses the lumped element circuit from figure 4.3, the CPW capac-

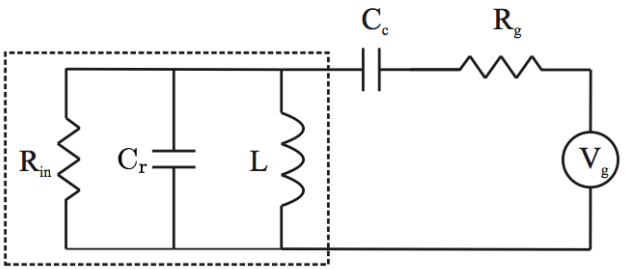

Figure 4.3: Lumped element resonance circuit. The resonator is connected to the power source through the coupling capacitance C_c.

itance C_r, inductance L and resistance R_{in} can written for the lowest resonance mode as [6]

$$C_r = \frac{C'l}{2} \tag{4.10}$$

$$L = \frac{8L'l}{\pi^2} \tag{4.11}$$

$$R_{in} = \frac{Z_0}{\alpha l} \tag{4.12}$$

with C' and L' the capacitance and inductance per unit length, Z_0 the characteristic impedance of the CPW and α the loss per unit length. The total resonance frequency is then $\omega_r = 1/\sqrt{L(C_r + C_c)}$.

The inductance per unit length is given by $L' = L'_{geo} + L'_{kin}$. The first term is the normal, geometric inductance and depends only on the geometry of the waveguide. The second term is the kinetic inductance and is due to the kinetic energy of the charge carriers. In HTS, the kinetic inductance is significant and has to be accounted for.

4.2 Design parameters

The conduction properties of (001) and (103) YBCO are very different. L_{kin} of the (103) resonator is much larger due to the larger London penetration depth in the transport direction (this is discussed in section 4.6.2). Therefore, two separate resonator designs are created: one for resonator 1-2 and one for resonator 3.

Several requirements have to be met: the correct value must be chosen for the characteristic impedance of the CPW, the resonance frequency of the resonator, and the coupling capacitance. These values are determined by the geometry and the dimensions of the resonators (figure 4.2).

4.2.1 The characteristic impedance

When the CPW is connected to the source, the characteristic impedance Z_0 of the different elements need to be matched to prevent unwanted reflections of electromagnetic waves. The standard value for all coaxial lines is $Z_0 = 50\Omega$, so the CPW must be designed in such a way to achieve the same value. The height of the conductor t and the substrate h (figure 4.2.b) are taken fixed with values of respectively 120 nm and 500 μm. The gap width g and the conductor width $2s$ must be larger than 10 μm to allow easy fabrication with photolithography.

If losses are neglected, the characteristic impedance Z_0 is calculated using both the capacitance C' and the inductance L' per unit length with

$$Z_0 = \sqrt{\frac{L'}{C'}} \tag{4.13}$$

C' and L' are calculated with conformal mapping [46, 47]. The matlab code is given in appendix C. The inductance L' depends on the London penetration depth of the conductor material. For resonator 1-2, $\lambda_{ab}(0)$ was taken 150 nm. Using parameters $g = 16\mu m$ and $2s = 37,6\mu m$, the characteristic impedance Z_0 becomes $48,67\Omega$, which is close enough to 50Ω. The resonator dimensions are listed in table 4.1. For the case of (103) YBCO $\lambda_{103}(0)$ is taken $1000nm$. If the parameters are set to $g = 10\mu m$ and

$s = 32\mu m$, the characteristic impedance Z_0 meets the required value of 50Ω. Figure 4.4 shows the dependence of Z_0 on λ_L.

	t	h	g	$2s$	l
Resonator 1-2	$120nm$	$500\mu m$	$16\mu m$	$37,6\mu m$	$4,8mm$
Resonator 3	$120nm$	$500\mu m$	$10\mu m$	$48\mu m$	$4,8mm$

Table 4.1: dimensions of the resonators with t the conductor thickness, h the height of the dielectric substrate, g the gap width, $2s$ the conductor width and l the resonator length as defined in figure 4.2.a.

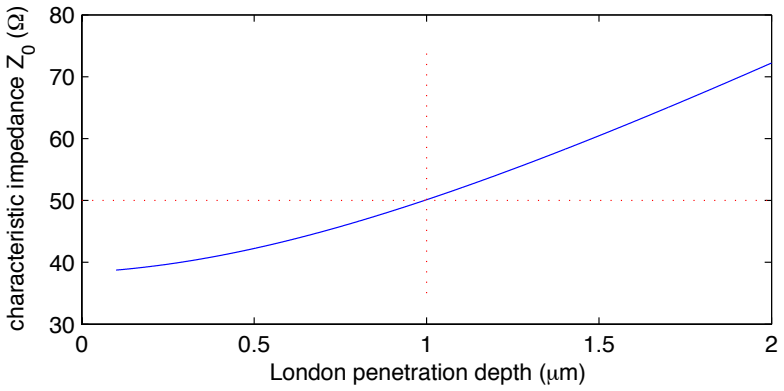

Figure 4.4: The characteristic impedance varies with the London penetration depth. In this calculation the dimensions are those of the 103 resonator.

4.2.2 The length of the resonator

The wavelength of the standing waves in the resonator is determined by the resonator length, but the resonance frequency ω_r is determined by the total capacitance and inductance of the CPW through equation (4.1). ω_r must be higher than the frequency of thermal photons created by thermal excitations so the thermal population of the resonator is $\ll 1$.

By choosing ω_r so that $\hbar\omega_r >> k_B T$, the thermal photons will not be able to resonate in the cavity. Filling in Plank constant h and Boltzmann constant k_B, a temperature of 50 mK would create photons of approximately 1GHz. Since the lowest measuring temperature will be around 300 mK, the resonance frequency should be larger than 6 GHz. Furthermore, the frequency should be lower than 8 GHz to use standard microwave equipment. A resonance frequency of $\omega_r = 6.4GHz$ is chosen.

With ω_r set, the length of the resonator can be calculated. The wave propagation

velocity in a transmission line can be written in two ways:

$$v_p = \frac{c}{\sqrt{\epsilon_{\text{eff}}}} = \frac{1}{\sqrt{L'C'}} \tag{4.14}$$

L' and C' are the inductance and capacitance per unit length, c the speed of light in vacuum and ϵ_{eff} the effective dielectric constant of the CPW calculated in appendix C. A value of $\epsilon_{\text{eff}} = 6.05$ was obtained for both resonator designs, but L_{kin} was neglected in this calculation.

The length of the resonator is determined with the relations (4.10) and (4.11):

$$l = \frac{\pi}{2} \frac{c\sqrt{LC}}{\sqrt{\epsilon_{\text{eff}}}} \tag{4.15}$$

Using equation (4.1) this becomes

$$l = \frac{\pi c}{2\omega_r \sqrt{\epsilon_{\text{eff}}}} \tag{4.16}$$

Since ϵ_{eff} is identical for both resonator designs, this gives a length of $4.8mm$. The results will show that L_{kin} could not be neglected, since resonator 3 has a lower resonance frequency than resonator 1 and 2.

4.2.3 Coupling capacitance

Microwave photons are injected in the resonator structure through the coupling capacitor C_c. The photons resonate in the cavity for an average amount of time $1/\kappa$ before they are absorbed by the conductor or the dielectric (internal losses), or they leak back out through the coupling capacitor (external losses). The value of C_c is calculated to obtain the external quality factor by equation (4.7).

An interdigital capacitor with two fingers is used to achieve a good coupling to the CPW resonator while keeping the feature size above $10\mu m$. The layout of the interdigital capacitor is depicted in figure 4.5. The dimensions are given in table 4.2.

	finger length	finger width	finger spacing
Resonator 1-2	$37.4\mu m$	$15\mu m$	$7.6\mu m$
Resonator 3	$16\mu m$	$21.5\mu m$	$4.9\mu m$

Table 4.2: dimensions of interdigitating coupling capacitors of the two resonator designs.

C_c was calculated using two different methods. The first one is a built-in model from *Microwave office*. The second method was developed by Spartak et al. and makes use of conformal mapping [48]. Furthermore, the coupling capacitance was calculated from from the measurement results in section 4.6.1. The results in table 4.3 show that the two models differ quite a lot, but from the measurements we see that the calculation of C_c is quite accurate with conformal mapping.

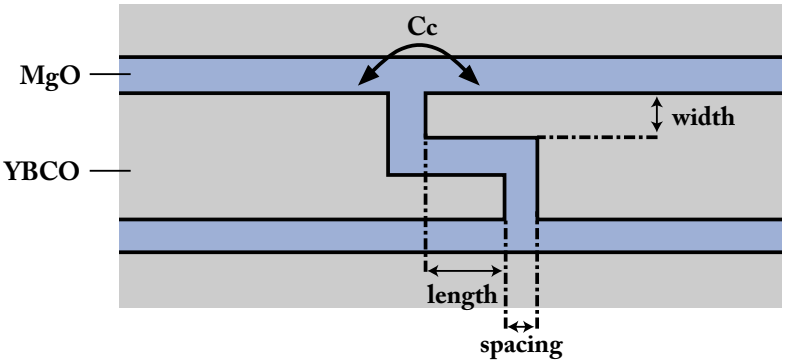

Figure 4.5: Top view of the interdigitating coupling capacitor with two fingers.

	Microwave office	conformal mapping	results section 4.6.1
Resonator 1-2	$4.15fF$	$8fF$	$7.8fF$
Resonator 3	$2.2fF$	$4.2fF$	/

Table 4.3: Calculations of the coupling capacitance

4.2.4 Shape of the resonator structure

The tables 4.1 and 4.2 summarize the differences between the designs for resonator 1-2 and resonator 3. There is however one more important difference due to the anisotropy of the YBCO crystal.

The (001) YBCO thin film is isotropic in the plane of the film, so the conduction properties are isotropic in the plane of the resonator. Subsequently there are no limitations on the shape of the CPW path. The (103) YBCO thin film is anisotropic in the plane of the resonator, and since the transport properties along the c-axis are investigated, conduction along the (*ab*)-planes should be avoided as much as possible. This implies that meandering should be avoided for the (103) YBCO resonator. The final resonator shapes are depicted on figure 4.6.

4.3 Fabrication of co-planar waveguide resonators

A short overview of the fabrication process is given below. The specific parameters for the recipe are given in appendix D.

4.3.1 Pulsed laser deposition

The parameters for the pulsed laser deposition of the three resonators are as follows:

- Resonator 1: YBCO is deposited directly on the MgO substrate to obtain a (001) orientation. A target with 5% higher Yttrium concentration is used to obtain a

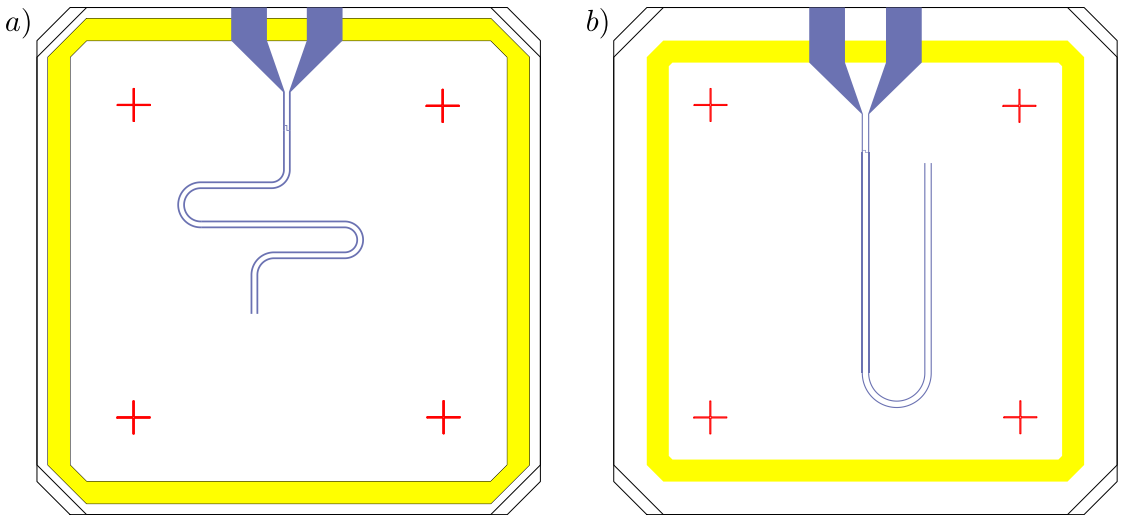

Figure 4.6: The $5x5mm$ MgO substrates are too small to fit the resonators when they are straight, so some meandering is required. For the (103) YBCO resonator meandering should be avoided due to the in-plane anisotropy of (103) YBCO.

higher green phase concentration.

- Resonator 2: YBCO is deposited directly on the MgO. A target with 5% lower Yttrium concentration is used to obtain a lower green phase concentration.

- Resonator 3: A 30 nm-seed layer of $SrTiO_3$ is deposited on the MgO substrate. YBCO is then deposited on the seed layer to obtain a (103) growth orientation.

4.3.2 Patterning of the resonator with photolithography and ion beam milling

A 150nm-thick gold layer is sputtered on the YBCO thin film with a FHR MS150 sputter tool. This is to prevent the out-diffusion of oxygen from the YBCO during the fabrication process. Furthermore, YBCO loses it's superconductive properties when it is brought in contact with solvents or resists.

The resonator structures shown in figure 4.6 are patterned with photolithography. A layer of photosensitive polymer (S1813 positive photoresist) is spun on the samples. The parts which must be removed are then exposed to UV light using a mask aligner. The exposed polymer molecules break due to the UV light, and are removed with a developer (MF-319). The minimum feature size of the resonators is $10\mu m$, and this can easily be achieved with photolithography. Smaller features are obtained using electron beam lithography.

The trenches are etched away with a CAIBE ion beam milling system from Oxford. The photoresist is removed using oxygen plasma etching (ashing). It may not be removed with acetone, since this would degrade the exposed YBCO. Furthermore the ion beam milling makes the resist very hard to dissolve.

Finally the protective gold layer is etched away using ion beam milling. Leftover gold would severely degrade the conduction properties of the resonator, since most of the AC current travels through the outer layers of the material due to the skin effect.

4.3.3 Wire bonding of the sample

Since it is difficult to attach gold wire bonds directly to the YBCO connection pads, an outer ring of gold is kept using an extra photolithography step. The wire bonding is necessary to make a good connection from the sample to the coaxial cable on the sample holder. A picture of one of the finished resonators is shown in figure 4.7.

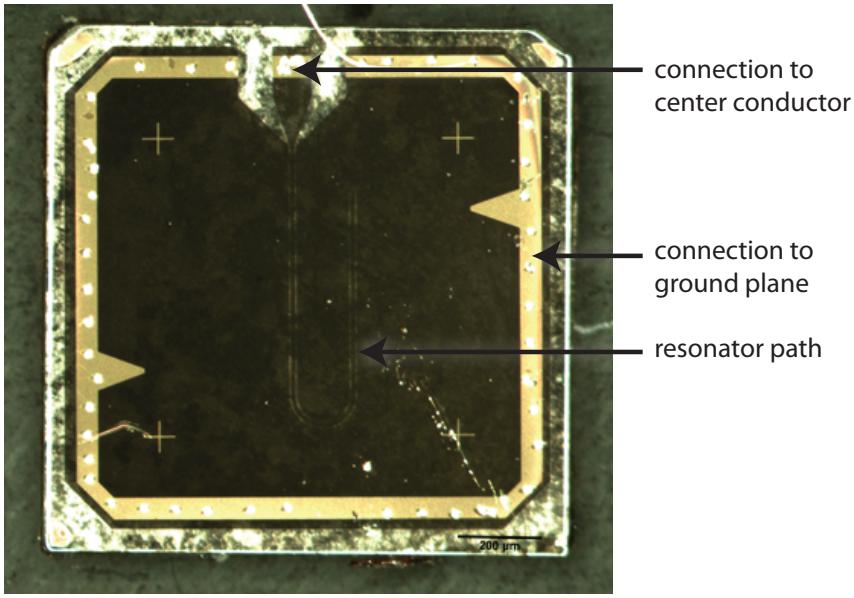

Figure 4.7: Picture of resonator 3 after the measurements were completed.

4.4 Cryogenics and microwave setup

The HelioxVL cryostat is used again to cool the samples down to millikelvin temperatures. It is connected to the vector network analyzer using a microwave coaxial cable. The working principle of the HelioxVL is explained in appendix A.4.

The microwave setup is depicted in figure 4.8. The microwave reflections are measured using a vector network analyzer. A directional coupler separates the input from the output, allowing for a strong attenuation at the input. To analyze Q in the low

power limit, an attenuator is placed between the power source and the sample, with attenuations from 0 up to -50dB. The directional coupler gives an additional attenuation of 30dB to the input signal, but no attenuation to the output, so an amplifier of 30dB boosts the signal back to it's original value.

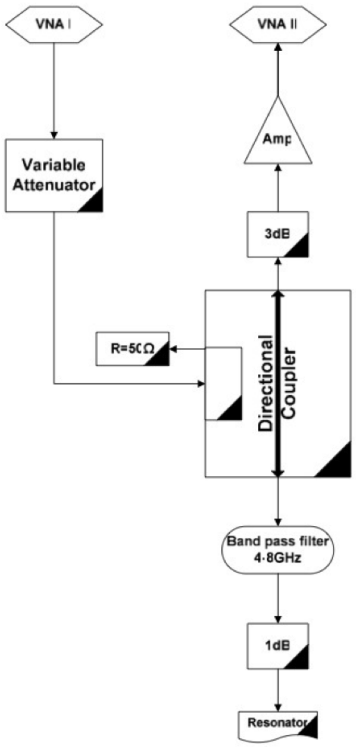

Figure 4.8: Schematic of the microwave setup, VNA I and VNA II are input and output of vector network analyzer.

4.5 The three coupling regimes

The properties of the thin film are determined by measuring the quality factor of the resonator at various temperatures between 300mK and 60K. As already mentioned in section 4.1, Q has two contributions: the external quality factor Q_{ext} and the internal quality factor Q_{int}. When the temperature is increased, the London penetration depth λ_L of the superconductor rises, and subsequently the kinetic inductance L_{kin} also rises. This has two effects:

1. The higher inductance L shifts the resonance frequency of the resonator to lower

values according to

$$\omega_r = \frac{1}{\sqrt{(L_{geo} + L_{kin}(T))C}} \tag{4.17}$$

In resonators 1-2, $L_{kin}(0)/L_{geo} = 0.03$ and this effect will not be noticable. In resonator 3, $L_{kin}(0)/L_{geo} = 0.53$ and the frequency shift is significant.

2. Q_{int} is lower: Current flows within a distance λ_L from the edges, and the surface resistance is proportional to λ_L^3. As it rises with the temperature the internal losses are higher.

Q_{ext} is temperature-independent. Therefore at higher temperatures $Q_{int} < Q_{ext}$, and the resonator is undercoupled. At lower temperatures the losses due to the coupling with the outside world dominate, and the resonator is overcoupled. This implies that at a certain temperature $Q_{int} = Q_{ext}$, and the resonator is critically coupled. At this point $Q_{ext} = 2Q$ can be measured, and with this value Q_{int} is calculated for all the other temperatures. Table 4.4 gives an overview of the coupling regimes.

When the resonator goes from the undercoupled to the overcoupled regime, the complex reflection undergoes a phase change of 2π. This is represented on the polar plot on figure 4.9. For each frequency the amplitude and phase of the complex reflection signal are plotted, and this trace gives rise to a circle. When the resonator is undercoupled the curve does not encircle the origin, leading to a small phase change at ω_r. When the resonator is overcoupled the phase change around ω_r is 2π, because the curve encircles the origin. When the resonator is critically coupled, the curve crosses the origin at the resonance frequency, leading a reflected signal with zero amplitude and a phase change of 2π.

coupling regime	temperature range	dominating losses	phase shift in reflection
overcoupling	low T	$Q_{int} > Q_{ext}$	2π
critical coupling		$Q_{int} = Q_{ext}$	
undercoupling	high T	$Q_{int} < Q_{ext}$	$< 2\pi$

Table 4.4: Summary of the coupling regimes

4.6 Measurement results and discussion

4.6.1 The internal quality factor

The critical coupling regime was reached at 48K for resonator 1 (the (001) YBCO resonator with higher Yttrium concentration). At this point the external quality factor could be calculated and a value of $Q_{ext} = 3265$ was obtained. The amplitude and the phase of the reflection signal are shown in figure 4.10 for several temperatures.

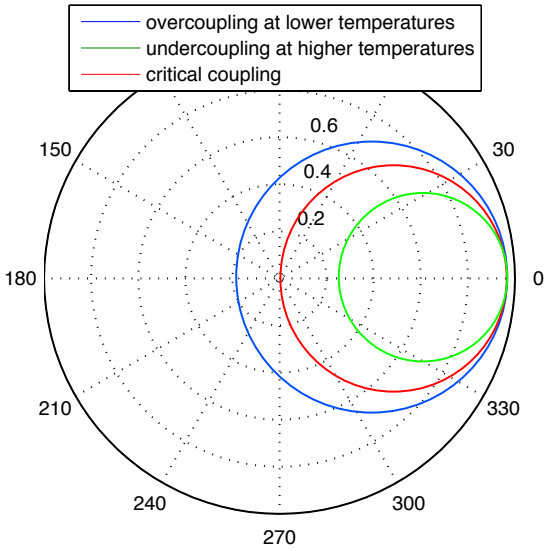

Figure 4.9: Polar plot of the reflection for undercoupled (red), overcoupled (blue) and critically coupled regime(green)

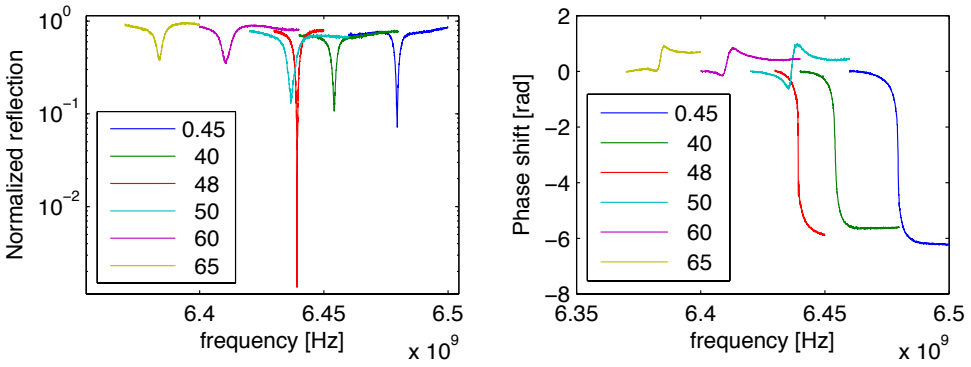

Figure 4.10: Amplitude and phase vs frequency of the reflected microwave signal for resonator 1. At 48K the reflection signal has 0 amplitude and a 2π phase shift at the resonance frequency, which means the resonator is critically coupled. ω_r shifts to smaller values when the temperature is higher.

The other two resonators were undercoupled for all temperatures. Resonator 2 had a problem during the photolithography: the mask did not make perfect contact with the sample, and the spacing of the capacitor was a bit larger leading to a lower coupling capacitance. Figure 4.11 shows the difference between interdigitating capacitors of resonator 1 and 2. However, resonator 2 is very close to critical coupling at very low temperatures, and a value of $Q_{ext} \approx 7000$ can be estimated. The coupling capacitance of the (103) resonator was designed too small, and the internal losses completely dominate

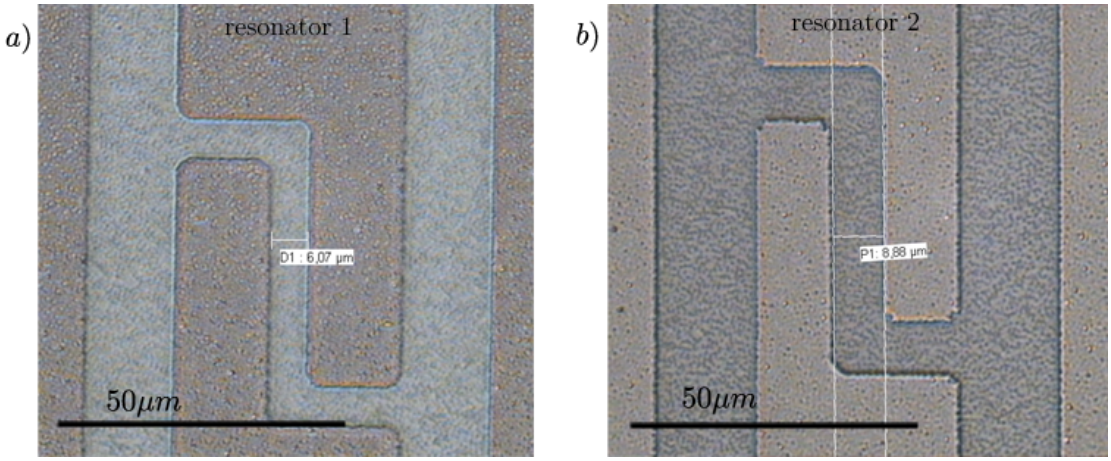

Figure 4.11: The coupling capacitance is smaller for resonator 2 (right) than for resonator 1 (left), giving a higher external quality factor.

the external losses. From microwave office and the conformal mapping technique a value around $Q_{ext} \approx 30000$ is estimated, and the external losses can be neglected.

The internal quality factor of the three resonators is shown in figure 4.12 for different temperatures. Values up to 5500 are obtained for resonator 1 and 2. Previous work

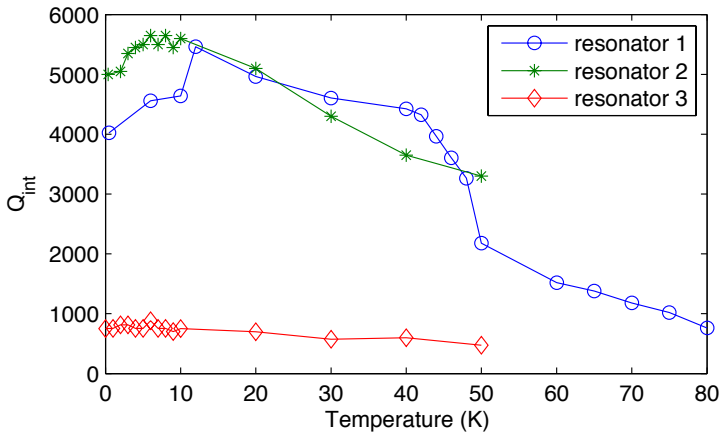

Figure 4.12: The internal quality factor of the three resonators

showed that high-quality resonators on MgO substrates have a similar Q_{int} [4]. From this we can conclude that the dissipation is mainly due to the MgO substrates, and (001) YBCO shows good conductive properties. Q_{int} is only slightly lower in resonator 1. This means the higher concentration of green phase does not have a significant influence on the dissipation. The quality factor of resonator 3 was much lower. This has several

causes:

1. The surface resistance is highly dependent on the London penetration depth ($R_s \sim \lambda_L^3$ [12]), which is much larger for resonator 3 in the transport direction.

2. There are many inclusions on the surface of (103) YBCO due to it's granular structure. This rough surface leads to a higher surface resistance.

All results for the quality factors are summarized in table 4.5.

	maximum Q_{int}	Q_{ext}
Resonator 1	5460	3265
Resonator 2	5650	7000
Resonator 3	882	30000

Table 4.5: Overview of the results for the quality factor

4.6.2 London penetration depth

The shift to smaller resonance frequencies can be used to extract the temperature dependence of the London penetration depth in the direction of the transport. This is quite interesting, since the temperature dependence is directly correlated to the order parameter of the superconductor. For resonator 1-2 the transport is fully in the (ab)-plane, and λ_{ab} is extracted. In resonator 3 the transport happens both in the c-axis direction and in the (ab)-planes. In general, the effective London penetration depth is given [49] by

$$\lambda_{\text{eff}}^2 = \lambda_{ab}^2 \cos^2\theta + \frac{1}{2}(\lambda_c^2 + \lambda_{ab}^2)\sin^2\theta \tag{4.18}$$

In resonator 3 the direction of the current is $\theta = 90°$ (figure 4.13), giving

$$\lambda_{103}^2 = \frac{1}{2}(\lambda_c^2 + \lambda_{ab}^2) \tag{4.19}$$

The temperature-dependence of λ_{ab} and λ_c is given by the Gorter- Casimir two fluid approximation with an arbitrary exponent n:

$$\lambda_L(T) = \frac{\lambda_L(0)}{\sqrt{1-(T/T_c)^n}} \tag{4.20}$$

The parameter $\lambda_L(0)$ depends strongly on the oxygen doping of the thin film, which can be determined with a T_c-measurement. Resonator 1 and 2 both reached T_c at 87K, giving a $\lambda_{ab}(0) = 158nm$ [50]. Resonator 3 has $T_c = 89K$, but $\lambda_c(0)$ is more difficult to determine from the literature. It was obtained from fitting the resonance frequency in the model at very low temperatures, and a value of $\lambda_c(0) = 1.6 \pm 0.1\mu m$ was obtained.

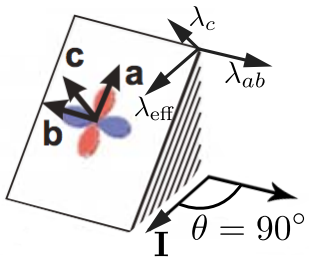

Figure 4.13: λ_{eff} depends on the direction of the current through the [103]-oriented film

The exponent n is obtained by fitting the variation in resonance frequency with the temperature using the equation:

$$\frac{f_r(T)}{f_r(0)} = \sqrt{\frac{L_{geo} + L_{kin}(0)}{L_{geo} + L_{kin}(T)}} \tag{4.21}$$

The fitting is shown in figure 4.14, and the results are

$$n_{ab} = 1.9 \pm 0.1 \qquad \lambda_{ab} = 158 \pm 10nm \tag{4.22}$$

$$n_c = 2.4 \pm 0.1 \qquad \lambda_c = 1.6 \pm 0.1\mu m \tag{4.23}$$

The temperature dependence of λ_c is much stronger than for λ_{ab}. These results are consistent with previous research in the group [49].

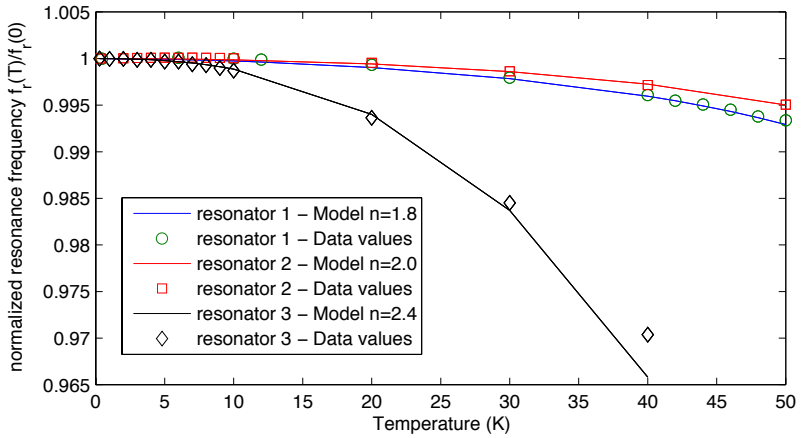

Figure 4.14: The curve fit of the normalized resonance frequency for the three resonators

4.6.3 Surface resistance

The surface resistance of superconductive co-planar waveguide is calculated using the quality factor and the London penetration depth [47,51]. In the thick-film limit ($t > \lambda_L$), the surface resistance is given by

$$R_s = \frac{\mu_0 \omega_r L' \lambda_L}{Q_{int} L'_{kin}} \tag{4.24}$$

But in the thin film limit ($t < \lambda_L$), the following equation should be used:

$$R_s = \frac{\mu_0 \omega_r L' \lambda_L}{Q_{int} L'_{kin}} \frac{\lambda_L}{t} \tag{4.25}$$

The kinetic inductance per unit length L'_{kin} is then calculated with

$$L'_{kin} = \mu_0 \frac{\lambda_L^2}{t} \frac{C'_1 + C'_2}{2s}$$

$$C'_1 = \frac{2}{\left[K(k_0)\right]^2} \cdot \frac{1}{1-k_0^2} \Big[1 + \frac{1}{4} \ln\Big(\frac{2s}{\lambda_\perp} - 1\Big) - \frac{k_0}{4} \ln\Big(\frac{2s+g-\lambda_\perp}{g+\lambda_\perp}\Big)\Big]$$

$$C'_2 = \frac{2}{\left[K(k_0)\right]^2} \cdot \frac{k_0}{1-k_0^2} \Big[1 + \frac{1}{4} \ln\Big(\frac{2(s+g)}{\lambda_\perp} + 1\Big) - \frac{1}{4k_0} \ln\Big(\frac{2s+g-\lambda_\perp}{g+\lambda_\perp}\Big)\Big]$$

with $k_0 = s/(s+g)$, $K(k_0)$ the complete elliptic integral of the first kind, and the edge London penetration depth $\lambda_\perp = 2\lambda_L^2(T)/t$.

At low temperatures, resonator 1 has a surface resistance of $R_s(0) = 39\mu\Omega$, and resonator 2 has $R_s(0) = 45\mu\Omega$. The slightly higher value of the latter one can be explained by the presence of insulating green phase in the YBCO thin film. Resonator 3 shows a much higher value of $R_s(0) = 661\mu\Omega$. Figure 4.15 shows that R_s rises with the temperature.

4.6.4 Low power regime

Depending on the quality of the YBCO thin film, there is a certain amount of unwanted two-level fluctuators in the resonator [24]. The exact nature of these fluctuators is still unknown, but they can be excited by absorbing a photon in the resonator (photon traps). In the high-photon or high-power limit, the two-level fluctuators will be equally distributed between the ground state and excited state, and extra photon losses due to these traps will not be present. A qubit however is operated at very low power, where almost all fluctuators are in the ground state. This means the absorption of photons by the two-level fluctuators is significant. Therefore it is important to know the amount of two-level fluctuators, and the quality factor will be measured in the low-photon limit.

The internal quality factor was measured at 300mK. The power was further reduced with a variable attenuator (from 0 to -50dB). The results are depicted in figure 4.16.

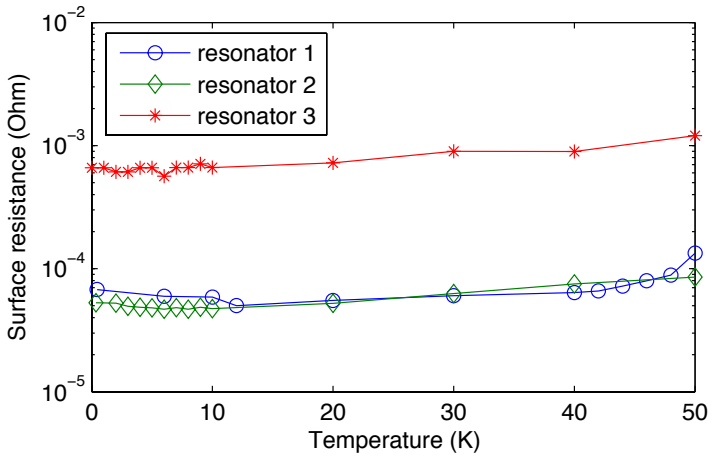

Figure 4.15: Surface resistance of the three resonators

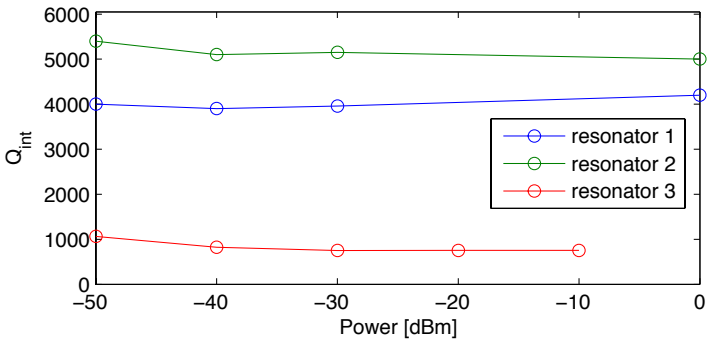

Figure 4.16: Q_{int} as a function of the injected power for the three resonators (with 0dBm=1mW).

For none of the resonators a significant drop in Q_{int} was observed at low powers. This could be due to different reasons:

To achieve the low-photon limit in the range of 6.4GHz, the temperature should be much lower than 320mK. If the temperature is higher than this value, thermal photons with frequencies around the resonance frequency are generated due to blackbody radiation, inducing thermal noise. The number of thermal photons is given by

$$\langle n_t \rangle = (e^{\frac{\hbar\omega}{k_B T}} - 1)^{-1} \tag{4.26}$$

For $k_B T < \hbar\omega$ the number of thermal photons inside the resonator is smaller than 1. Ideally, the temperature should be reduced further, e.g. with a dilution fridge.

Secondly, the effect will only be noticeable if the amount of 2-level fluctuators is comparable to the number of photons in the resonator. The injected power is -20dBm ($= 0,01mW$), and the signal is further attenuated by the directional coupler ($-30dB$),

the wirings ($-10dB$) and the variable attenuator ($-50dB$). This gives a total $-110dB$ or $1 \cdot 10^{-11} mW$. The average number of photons is then calculated as follows:

$$Q = \frac{\text{Energy stored}}{\text{Energy dissipated per radian}} = \frac{\langle n \rangle \hbar \omega_r}{P_{int}/\omega_r} \tag{4.27}$$

$$\langle n \rangle = \frac{Q\,P}{\hbar \omega^2} = \frac{4000 \cdot 1 \cdot 10^{-14}}{1 \cdot 10^{-34} \cdot (2\pi \cdot 6.4 \cdot 10^9)^2} \approx 10^4 \tag{4.28}$$

The power should be further reduced untill $\langle n \rangle \approx 1$ to clearly see the effects of the two-level fluctuators. In the current experiment, the input signal could not be further attenuated due to the low signal to noise ratio (S/N) at the output. A solution would be to use a cryogenic amplifier. Moreover, the experiments would take a very long time due to the many averages needed to measure the reflection signal.

Appendix A

Different tools for the study of YBCO thin films

A.1 X-Ray diffractometry

X-ray diffractometry (XRD) is used to verify the crystal structure of the deposited YBCO thin film. X-rays are emitted from a source, they interact with the sample and are reflected towards a detector. The interaction with the sample is described by Braggs law:

$$n \cdot \lambda = 2d \cdot \sin\theta \quad n = 1, 2, 3, \ldots \tag{A.1}$$

λ is the wavelength of the X-rays, θ is the angle of the incoming X-rays and d is the distance between the atomic planes. For certain angles the reflected X-rays interfere constructively, and this is registered with the detector(figure A.1). By sweeping over different angles the crystal structure of the material is determined.

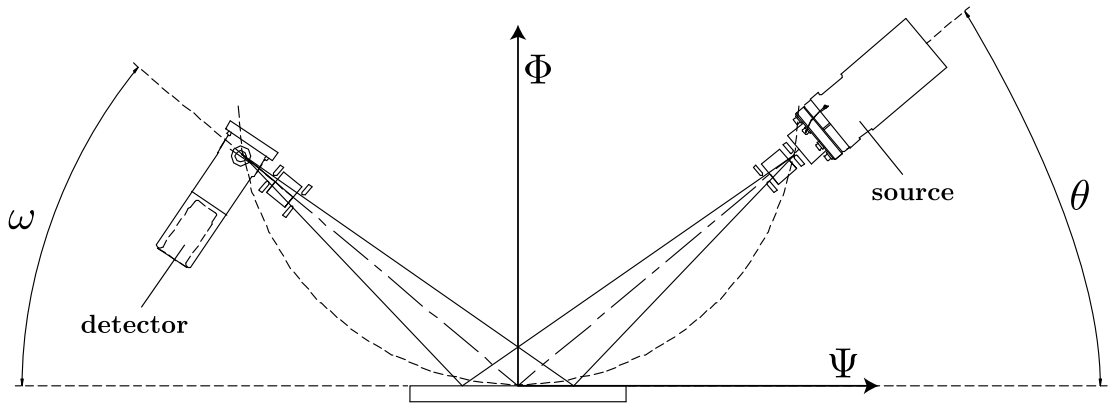

Figure A.1: Illustration of the XRD setup

Several scanning modes are possible are possible with XRD:

2θ-ω scan In this mode (also called Bragg-Bentano), the source sweeps over all the angles to find the Bragg planes of the crystal. The detector is kept at the same angle as the source (θ=ω). This one-dimensional scan reveals the different crystal orientations.

Φ scan Here the sample is rotated along the Φ-axis. Φ is the angle between the $\hat{a}$- and $\hat{b}$-axes of the YBCO and the $[0\bar{1}0]$ direction of MgO. This scan reveals the in-plane alignment of a film with respect to the sample.

Ψ-2θ-ω scan This two-dimensional scan (also called mapping) is a collection of 2θ-ω scans while the sample is rotated along the Ψ-axis. It reveals information about the crystallinity of the material. If sharp peaks are obtained only for a narrow range of Ψ-values, the film is mono-crystalline.

A.2 Scanning electron microscopy

In a scanner electron microscope a focused beam of high-energy electrons scans over the surface of the sample. The electrons interact with the upper layers of the sample and secondary electrons are ejected out of the sample. The primary and secondary electrons give information about chemical composition, surface topography and crystallography. The analysis with SEM is very fast but it cannot be used for the analysis of small features, since the bombardment of high-energy electrons can easily destroy them.

A.3 Atomic force microscopy (AFM)

In atomic force microscopy a sharp probe scans over the surface of the sample and measures surface properties and the elevation profile of the sample. The probe has a radius of curvature on the order of nanometers, allowing analysis with atomic resolution. It is attached to a cantilever beam, and the deflection of this beam is registered with a laser as in figure **??**. The movement of the tip is regulated by piezoelectric actuators. When the AFM is operated in tapping mode the tip oscillates over the surface. The amplitude and the frequency of the oscillations are determined by the structure of the surface. This allows for high-resolution imaging of the surface with only minimal damage.

A.4 Working principle of the HelioxVL

There are 3 different phases to reach the base temperature.

In the first phase a temperature of 4.2K is obtained by inserting the cryostat in a liquid ^{4}He dewar. ^{4}He exchange gas inside the inner vacuum can (IVC) is used to conduct the heat away to the liquid ^{4}He.

In the second phase a sample temperature of approximately 1.6K is reached. The exchange gas is pumped out and a vacuum is applied to the 1K pot. Liquid ^{4}He is pumped from the dewar through a capillary to the 1K pot by opening the needle valve.

The liquid ^{4}He starts to evaporate, extracting the necessary heat from the 1K pot. ^{3}He vapor then condenses on the 1K pot and is collected in ^{3}He pot. The sample, which is mounted directly underneath it, is cooled further by the ^{3}He. Phase 2 and 3 are depicted in figure A.2.

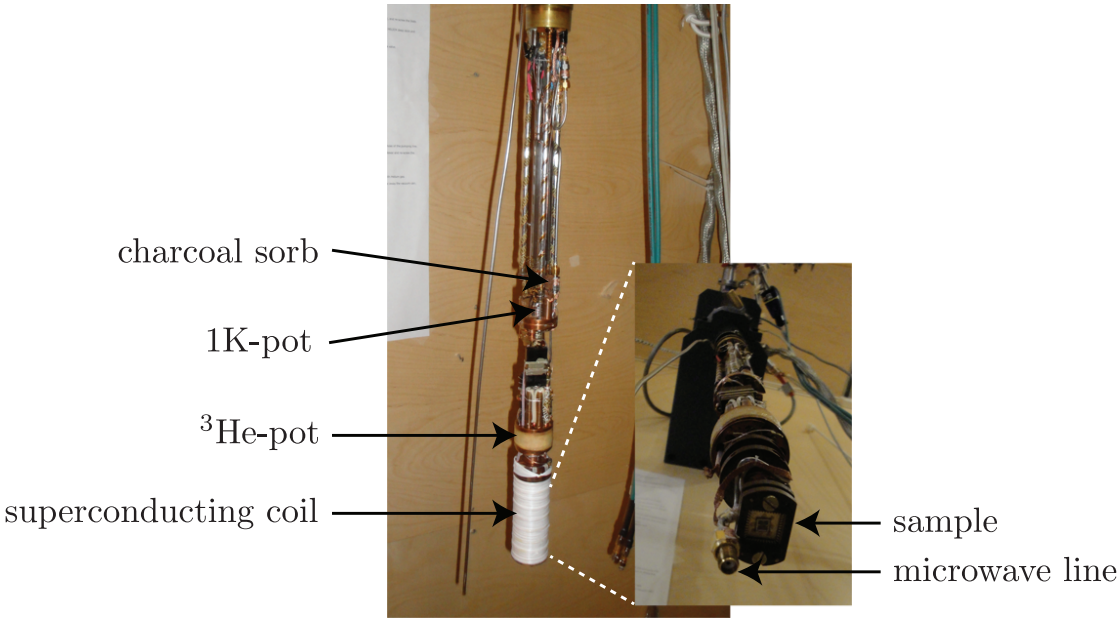

Figure A.2: The HelioxVL cryogenic system

In the third phase, a temperature of 300mK is achieved by an internal cooling mechanism that makes use of a charcoal sorb. When the sorb is cooled down it absorbs the ^{3}He vapor, thus lowering the vapor pressure of the liquid ^{3}He. The evaporation from the ^{3}He-pot lowers the sample temperature until 300mK. It can be kept cool for several hours, until all of the liquid ^{3}He is evaporated.

Appendix B

Determining the quality factor from the reflection signal

In this appendix, the equations are derived which are used to extract the quality factor Q from the reflection signal. The complex reflection on the resonator is defined by the characteristic impedance of the resonator (Z_L) and the characteristic impedance of the feeding line (typically $Z_0 = 50\Omega$)

$$\Gamma = \frac{Z_L - Z_0}{Z_L + Z_0} \tag{B.1}$$

If one considers the lumped element representation from figure B.1, equation (B.1) can be rewritten [52] as

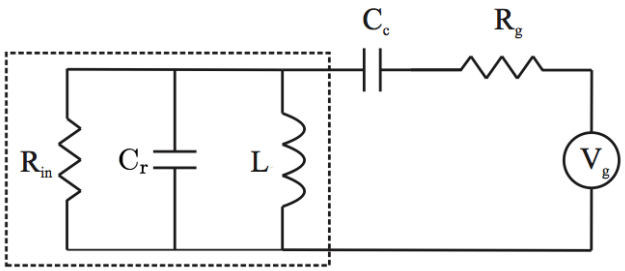

Figure B.1: lumped element resonance circuit

$$\Gamma(\omega) = \frac{1 - \omega^2 L\Big[C_r + C_c(1 - Z_0/R)\Big] + i\omega\big[L/R - C_c Z_0(1 - \omega^2 L C_r)\big]}{1 - \omega^2 L\Big[C_r + C_c(1 + Z_0/R)\Big] + i\omega\big[L/R + C_c Z_0(1 - \omega^2 L C_r)\big]} \tag{B.2}$$

Assuming $R \gg Z_0 = 50\Omega$, this becomes

$$\Gamma(x) = \frac{1 - x^2 + ix\big[Q_{int}^{-1} - \frac{1-kx^2}{1-k} Q_{ext}^{-1}\big]}{1 - x^2 + ix\big[Q_{int}^{-1} + \frac{1-kx^2}{1-k} Q_{ext}^{-1}\big]} \tag{B.3}$$

with $x = \omega/\omega_0$ and $k = C/(C_r + C_c)$. Under the assumption $\omega_0 C_c Z_0 \ll 1$ the resonance frequency is $\omega_0 = \sqrt{L(C_r + C_c}^{-1}$ and the internal and external quality factors are defined by

$$Q_{int} \simeq \omega_0 R_{in}(C_r + C_c)$$

$$Q_{ext} \simeq \frac{C_r + C_c}{\omega_0 Z_0 C_c^2}$$

Assuming $Q = (Q_{int}^{-1} + Q_{ext}^{-1})^{-1} \gg 1$ around x=1, equation (B.3) becomes

$$\Gamma(x) = \frac{1 - x^2 + ix\left[Q_{int}^{-1} - Q_{ext}^{-1}\right]}{1 - x^2 + ix\left[Q_{int}^{-1} + Q_{ext}^{-1}\right]} \tag{B.4}$$

In the critical coupling regime ($Q_{int} = Q_{ext}$), Q can be extracted from the resonance peak (figure B.2):

$$\left|\Gamma(1 + \frac{1}{2Q})\right| \simeq \frac{1}{\sqrt{2}} \tag{B.5}$$

Far away from the critical coupling regime ($Q_{int} \gg Q_{ext}$ and $Q_{int} \ll Q_{ext}$), Q is determined by

$$\frac{1 - \left|\Gamma(1 + \frac{1}{2Q})\right|}{1 - \left|\Gamma(1)\right|} = \frac{1 - \left|\Gamma(1 + \frac{1}{2Q})\right|}{1 - Q\left|Q_{ext}^{-1} - Q_{int}^{-1}\right|} \simeq \frac{1}{2} \tag{B.6}$$

Therefore, equation (4.3) is only valid away from the critical coupling regime.

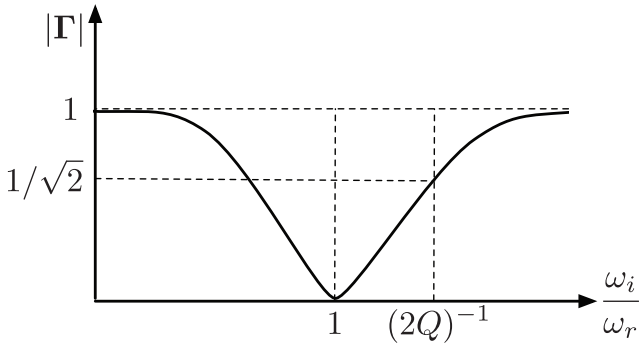

Figure B.2: In the critical coupling regime Q can be determined as shown. Equation (4.3) is no longer valid.

Appendix C

Matlab calculation of the characteristic impedance Z_0

According to Spartak et al. [46], the capacitance per unit length for an unshielded monolayered coplanar waveguide (CPW) is calculated using the following matlab code

```
k0 = s/(s + g);
k0inv = sqrt(1 - k0^2);
k1 = sinh(pi*s/(2*h1))/sinh(pi*(s+g)/(2*h));
k1inv = sqrt(1 - k1^2);
K0 = ellipke(k0);
K0inv = ellipke(k0inv);
K1 = ellipke(k1);
K1inv = ellipke(k1inv);
eps_eff = 1 + (eps_r - 1)/2 * K1/K1inv * K0inv/K0 Ctot = ...
   ... 4*eps0 * eps_eff * K0/K0inv;
```

The function `ellipke` is the complete elliptical integral of first kind, `eps_r` is the relative dielectric constant of the substrate ϵ_r, `eps0` is the dielectric constant of free space ϵ_0 and the parameters `s`, `g` and `h` are as defined in figure 4.2. The numerical values used are given in table 4.1.

According to Rauch et al. [47], the inductance per unit length is calculated by taking the sum of the external inductance L_{ex} and the kinetic inductance L_{kin} due to the inertia of the Cooper pairs. It is calculated with the following Matlab code

```
A = -t/pi + 0.5 * sqrt((2*t/pi)^2 + (2*s)^2);
B = (2*s)^2/(4*A);
C = B - t/pi + sqrt((t/pi)^2 + 0.25 * (2*g)^2);
D = 2*t/pi + C;
lambda_L = lambda_L_0/sqrt(1-(T/TC)^1.75);
Lex = mu0/4 * K0inv/K0;
Lkin = mu0*lambda_L*C/(4*A*D*K0) * (1.7/sinh(t/(2*lambda_L)) + ...
```

```
   ... 0.4/sqrt(((B/A)^2 - 1)*(1- (B/D)^2)));
Ltot = Lex + Lkin;
```

`lambda_L_0` is the London penetration depth at 0 Kelvin $\lambda_L(0)$, `lambda_L` is the temperature dependent London penetration depth and is approximated [49] by $\lambda_L(0)/\sqrt{1-(T/Tc)^n}$ with n between 1.5 and 2, `TC` is the superconductor critical temperature T_c and `mu0` is the magnetic permeability of free space μ_0.

Appendix D

Recipes

D.1 Pulsed laser deposition and ion beam milling

The substrates used are 5x5mm MgO substrates with a 6° vicinal cut. To ensure a high quality MgO surface, they are cleaned in acetone and residual particles are removed with a cotton swab and ultrasound vibrations. The substrate is then glued to the heater of the *TWIN* system for pulsed laser deposition. MgO substrates are very hydrophobic and easily absorb water from the ambient air. Therefore a few nanometers of the surface are etched away with ion beam milling function of the *TWIN* system. The standard recipe for ion beam milling involves four steps:

	Gas	Beam Voltage	Beam current	Etch time	Acc. Voltage
1	Ar	$300V$	$15mA$	$240s$	$380V$
2	$Ar + O_2$	$300V$	$15mA$	$120s$	$380V$
3	O_2	$300V$	$15mA$	$120s$	$380V$
4	O_2	$100V$	$10mA$	$240s$	$320V$

Table D.1: TWIN system ion beam milling parameters (standard recipe)

After ion beam milling, the substrate is heated to deposition temperature T_{dep} and the oxygen pressure in the chamber is brought to p_{dep}. $SrTiO_3$ and YBCO are deposited with the following parameters:

Material	T_{dep} $[°C]$	p_{dep} $[mbar]$	ϵ $[J/cm^2]$	ν_{pulse} $[Hz]$	cooldown rate $[°C/h]$
$SrTiO_3$	720	0.2	1.89	1	900
YBCO	770-840	0.6	1.89	10	600

Table D.2: TWIN system deposition parameters: deposition temperature, deposition pressure, laser pulse energy density, laser pulse frequency and cooldown rate. For the deposition of YBCO targets of different compositions have been used.

The films are cooled slowly under 800mbar oxygen pressure to meet the required oxygen doping. A YBCO film with thickness 130nm is achieved with 1120 pulses, and

an $SrTiO_3$ film of 30nm is achieved with 400 pulses. The thickness of $SrTiO_3$ is reduced to 15nm with in-situ ion beam milling. This etching steps promotes the growth of pure (103) YBCO. Moreover, the microstructure of the grain boundary is more reproducible with a thinner seed layer.

D.2 Patterning of the resonator structure

After pulsed laser deposition of YBCO, the following recipe is followed to pattern the resonator structure:

1. Sputtering of 150nm gold film: 150 seconds at $5 \cdot 10^{-3}$ mbar with *FHR MS150* sputter tool
2. Deep UV photolithography
   - Spinning of photoresist S1813 at 7000 rpm for 90 seconds
   - Pre-baking at 90° for 300 seconds
   - Deep UV exposure for 40 seconds
   - Development with MF-319 for 20 seconds
3. Ion beam milling of resonator trenches with *CAIBE Oxfor Ionfab*. Etching at 300V beam voltage, 7mA beam current, and $2.3 \cdot 10^{-4}$ mbar. The etch angle is 5°and the sample rotation is on.
   - Gold+YBCO trench etching: 138 minutes
   - Gold rim etching: 26.5 minutes
4. Resist removal with *Plasma Therm BatchTop* oxygen plasma etching: 20 minutes at 50W

Acknowledgements

This thesis was conducted in the master program Erasmus Mundus Master: Nanotechnology and Nanoscience. I spent the first year in KULeuven University in Belgium, and the second year in Chalmers Tekniska Högskola in Sweden.

This thesis has introduced me into the world of research, and it would not have been possible without a lot of people: I would like to thank Thilo and Floriana for guiding me through this whole experience and being such good supervisors. Shahid and especially David helped me a lot during the fabrication and revealed all the secrets of the clean room to me. Luca gave me the opportunity to do noise measurements and was a good friend. Thanks to all the other members of QDP such as Justin, Niclas, Fredrik, Sebastian, and Serge for the help, the nice work environment and the champagne/maple syrup breaks. The little Antoine and Sofia dramatically decreased the average age in the lab and made me feel more comfortable. Thanks to the Erasmus mundus nano programme, Guido Groeseneken and Per Rudquist for making this master possible. To Steven, Tim, Federico, Hugo, Ameha, Calin and Michael: thank you nanonerds, you made this erasmus an awesome, life-changing experience!

Finally I would also like to thank my parent for their never-ending support and motivation, and Dorien for making life wonderful. Because in the end, d-wave order parameters are just flowers!

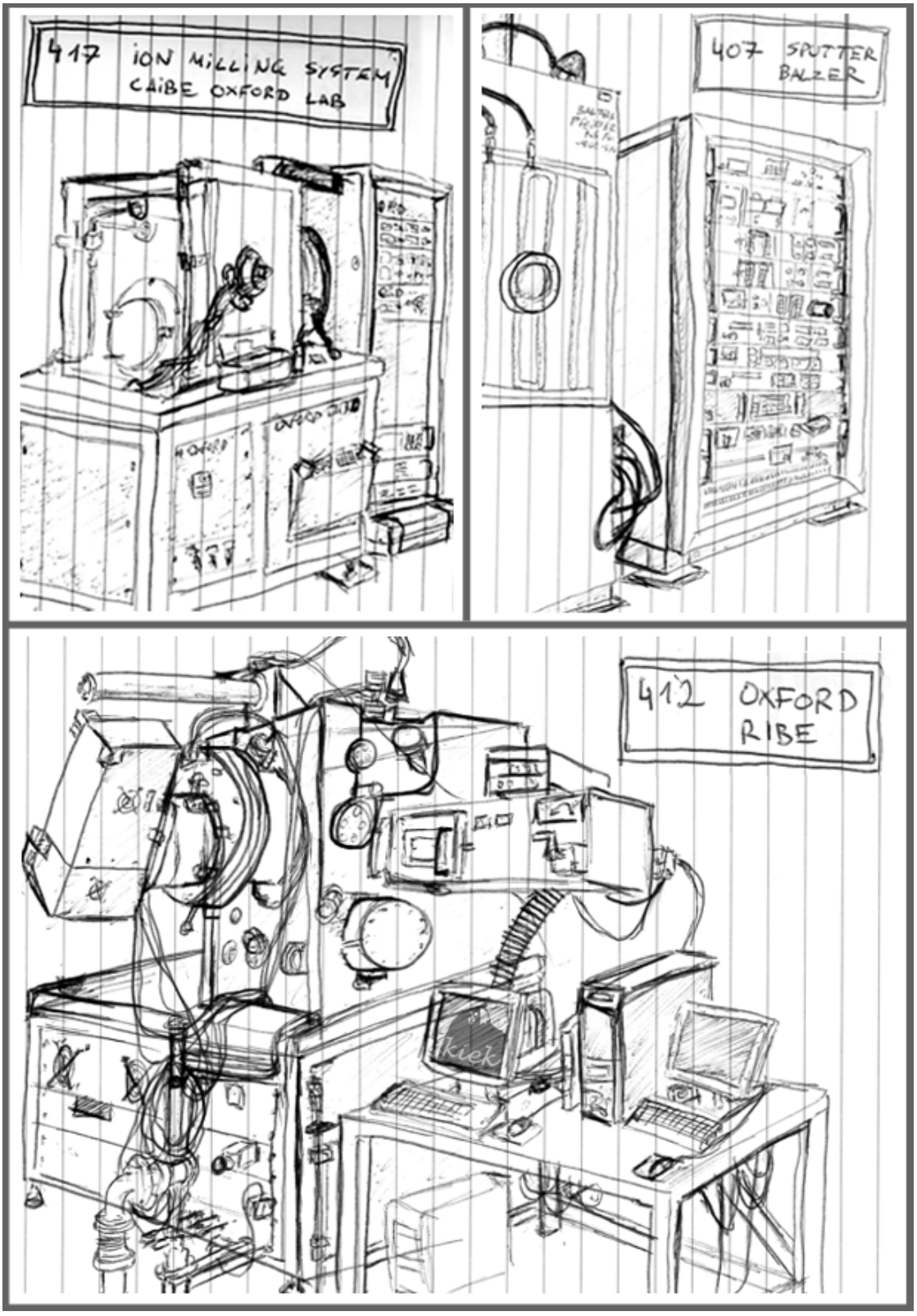
417 ION MILLING SYSTEM
CAIBE OXFORD LAB
407 SPUTTER
BALZER
412 OXFORD
RIBE

Bibliography

[1] Thilo Bauch, Tobias Lindstrom, Francesco Tafuri, Giacomo Rotoli, Per Delsing, Tord Claeson, and Floriana Lombardi. Quantum Dynamics of a d-Wave Josephson Junction. *Science*, 311(5757):57–60, 2006.

[2] Floriana Lombardi, Thilo Bauch, Karin Cedergren, Jesper Johansson, Tobias Lindström, Francesco Tafuri, Giacomo Rotoli, Per Delsing, and Tord Claeson. Energy level quantization in a yba2cu3o7-[delta] josephson junction. *Physica C: Superconductivity*, 460-462(Part 1):335 – 338, 2007. Proceedings of the 8th International Conference on Materials and Mechanisms of Superconductivity and High Temperature Superconductors - M2S-HTSC VIII.

[3] Beniamino Iandolo. *Nanosize HTS Josphson Junctions by a new self-assembly technique.* PhD thesis, Facolta di Ingegneria dei Sistemi, 2009.

[4] Mudassar Mumtaz Vrik. *High Frequency Properties of the Oxide materials at millikelvin temperatures for THS devices in the quantum limit.* PhD thesis, Chalmers university of technology, Göteborg, Sweden, 2009.

[5] K. Cedergren. *Grain Boundary Josephson pi-Junctions - Correlation between microstructure and transport properties for novel devices.* PhD thesis, Chalmers university of technology, 2010.

[6] Martin Sandberg. *Fast-tunable resonators and quantum electrical circuits.* PhD thesis, Chalmers university of technology, 2009.

[7] Leon N. Cooper. Bound electron pairs in a degenerate fermi gas. *Phys. Rev.*, 104(4):1189–1190, Nov 1956.

[8] Michael. Tinkham. *Introduction to superconductivity / Michael Tinkham.* McGraw-Hill, New York, 1975.

[9] K. A. Müller J. G. Bednorz. Possible hightc superconductivity in the balacuo. *Zeitschrift für Physik B Condensed Matter*, 64(2):189–193, june 1986.

[10] C. C. Tsuei and J. R. Kirtley. Pairing symmetry in cuprate superconductors. *Rev. Mod. Phys.*, 72(4):969, Oct 2000.

[11] Yuriy Makhlin, Gerd Schön, and Alexander Shnirman. Quantum-state engineering with josephson-junction devices. *Rev. Mod. Phys.*, 73(2):357–400, May 2001.

[12] Ted Van Duzer and Charles W. Turner. *Principles of superconductive devices and circuits, (second ed.)*. Prentice Hall PTR, 1999.

[13] B. D. Josephson. Possible new effects in superconductive tunnelling. *Physics Letters*, 1(7):251 – 253, 1962.

[14] P. W. Anderson and J. M. Rowell. Probable observation of the josephson superconducting tunneling effect. *Phys. Rev. Lett.*, 10(6):230–232, Mar 1963.

[15] Robert M. White Reviewer. Physics and applications of the josephson effect by a. barone and g. paterno. *Journal of Vacuum Science and Technology*, 21(4):1050–1051, 1982.

[16] Jens Koch, Terri M. Yu, Jay Gambetta, A. A. Houck, D. I. Schuster, J. Majer, Alexandre Blais, M. H. Devoret, S. M. Girvin, and R. J. Schoelkopf. Charge-insensitive qubit design derived from the cooper pair box. *Phys. Rev. A*, 76(4):042319, Oct 2007.

[17] M. H. Devoret, A. Wallraff, and J. M. Martinis. Superconducting qubits: A short review, 2004.

[18] J. Aumentado J. M. Martinis, S. Nam and C. Urbina. Rabi oscillations in a large josephson-junction qubit. *Phys. Rev. Lett*, 89(117901), 2002.

[19] J. E. Mooij, T. P. Orlando, L. Levitov, Lin Tian, Caspar H. van der Wal, and Seth Lloyd. Josephson persistent-current qubit. *Science*, 285(5430):1036–1039, 1999.

[20] P. Joyez D. Esteve V. Bouchiat, D. Vion and M. H. Devoret. Quantum coherence with a single cooper pair. *Phys. Scr.*, T T76(165), 1998.

[21] Y. A. Pashkin Y. Nakamura and J. S. Tsai. Coherent dynamics of a flux qubit coupled to a harmonic oscillator. *Nature*, 398(786), 1999.

[22] K. Bladh L. F. Spietz D. Gunnarsson P. Delsing K. W. Lehnert, B. A. Turek and R. J. Schoelkopf. Measurement of the excited-state lifetime of a microelectronic circuit. *Physical Review Letters*, 90(2), 2003.

[23] Alexandre Blais Alexandre Zagoskin. Superconducting qubits.

[24] John M. Martinis, K. B. Cooper, R. McDermott, Matthias Steffen, Markus Ansmann, K. D. Osborn, K. Cicak, Seongshik Oh, D. P. Pappas, R. W. Simmonds, and Clare C. Yu. Decoherence in josephson qubits from dielectric loss. *Phys. Rev. Lett.*, 95(21):210503, Nov 2005.

[25] MH Devoret. *Quantum fluctuations in electrical circuits*, volume 63. Elsevier Science Publ B V, 1997.

[26] A. Houck, Jens Koch, M. Devoret, S. Girvin, and R. Schoelkopf. Life after charge noise: recent results with transmon qubits. *Quantum Information Processing*, 8(2):105–115, 06 2009.

[27] D. J. Van Harlingen, T. L. Robertson, B. L. T. Plourde, P. A. Reichardt, T. A. Crane, and John Clarke. Decoherence in josephson-junction qubits due to critical-current fluctuations. *Phys. Rev. B*, 70(6):064517, Aug 2004.

[28] M. K. Wu, J. R. Ashburn, C. J. Torng, P. H. Hor, R. L. Meng, L. Gao, Z. J. Huang, Y. Q. Wang, and C. W. Chu. Superconductivity at 93 k in a new mixed-phase y-ba-cu-o compound system at ambient pressure. *Phys. Rev. Lett.*, 58(9):908–910, Mar 1987.

[29] Thomas P Sheahen. *Introduction to high-temperature superconductivity.* Selected topics in superconductivity. Plenum, New York, NY, 1994. Includes summaries.

[30] J. R. Waldram. *Superconductivity of metals and cuprates.* CRC Press, 1996.

[31] F. Tafuri, F. Carillo, F. Lombardi, F. Miletto Granozio, F. Ricci, U. Scotti di Uccio, A. Barone, G. Testa, E. Sarnelli, and J. R. Kirtley. Feasibility of biepitaxial $yba2cu3o7 - x$ josephson junctions for fundamental studies and potential circuit implementation. *Phys. Rev. B*, 62(21):14431–14438, Dec 2000.

[32] D. Dimos, P. Chaudhari, J. Mannhart, and F. K. LeGoues. Orientation dependence of grain-boundary critical currents in $yba2cu3o7 - \delta$ bicrystals. *Phys. Rev. Lett.*, 61(2):219–222, Jul 1988.

[33] K. Char, M. S. Colclough, S. M. Garrison, N. Newman, and G. Zaharchuk. Biepitaxial grain boundary junctions in yba2cu3o7. *Applied Physics Letters*, 59(6):733 –735, aug 1991.

[34] Julia M. Phillips. Substrate selection for high-temperature superconducting thin films. *Journal of Applied Physics*, 79(4):1829–1848, 1996.

[35] M. A. Hein. *High-Temperature Superconductor Thin Films at Microwave Frequencies, (*, volume 155. Springer, New York, 1999.

[36] U. Scotti di Uccio, F. Lombardi, and F. Miletto Granozio. Structural properties of single-domain (103) ybco films grown on buffered (110) mgo. *Physica C: Superconductivity*, 323(1-2):51 – 64, 1999.

[37] S. Nawaz M. Mumtaz G. Signorello F. Lombardi D. Gustafsson, T. Bauch. Low capacitance hts junctions for single electron transistors. *Physica C: Superconductivity (to be published)*, 2009.

[38] F. Herbstritt, T. Kemen, A. Marx, and R. Gross. Ultraviolet light assisted oxygenation process for submicron yba[sub 2]cu[sub 3]o[sub 7 - delta] thin film devices. *Journal of Applied Physics*, 91(8):5411–5418, 2002.

[39] U. Scotti di Uccio, F. Miletto Granozio, A. Di Chiara, F. Tafuri, O. I. Lebedev, K. Verbist, and G. van Tendeloo. Phase competition between y2bacuo5 and y2o3 precipitates in y-rich ybco thin films. *Physica C: Superconductivity*, 321(3-4):162 – 176, 1999.

[40] C. T. Rogers and R. A. Buhrman. Composition of $1f$ noise in metal-insulator-metal tunnel junctions. *Phys. Rev. Lett.*, 53(13):1272–1275, Sep 1984.

[41] A. Marx, L. Alff, and R. Gross. Low frequency voltage noise in high temperature superconductor josephson junctions. *Applied Superconductivity, IEEE Transactions on*, 7(2):2719 –2722, jun 1997.

[42] F. Ichikawa, T. Yamamoto, Y. Horie, T. Fukami, and T. Aomine. Random telegraph signal of sns bridges and high tc superconducting oxide thin films. *Physica C: Superconductivity*, 185-189(Part 4):2547 – 2548, 1991.

[43] M. Kawasaki, P. Chaudhari, and A. Gupta. 1/f noise in $yba2cu3o7 - \delta$ superconducting bicrystal grain-boundary junctions. *Phys. Rev. Lett.*, 68(7):1065–1068, Feb 1992.

[44] A. H. Miklich, John Clarke, M. S. Colclough, and K. Char. Flicker (1/f) noise in biepitaxial grain boundary junctions of yba2cu3o7-x. *Applied Physics Letters*, 60(15):1899 –1901, apr 1992.

[45] Peter A. Rosenthal, M. R. Beasley, K. Char, M. S. Colclough, and G. Zaharchuk. Flux focusing effects in planar thin-film grain-boundary josephson junctions. *Applied Physics Letters*, 59(26):3482–3484, 1991.

[46] S. Gevorgian, L.J.P. Linner, and E.L. Kollberg. Cad models for shielded multilayered cpw. *Microwave Theory and Techniques, IEEE Transactions on*, 43(4):772 –779, apr 1995.

[47] W. Rauch, E. Gornik, G. Solkner, A. A. Valenzuela, F. Fox, and H. Behner. Microwave properties of yba2cu3o7-x thin films studied with coplanar transmission line resonators. *Journal of Applied Physics*, 73(4):1866 –1872, feb 1993.

[48] S.S. Gevorgian, T. Martinsson, P.L.J. Linner, and E.L. Kollberg. Cad models for multilayered substrate interdigital capacitors. *Microwave Theory and Techniques, IEEE Transactions on*, 44(6):896 –904, jun 1996.

[49] J. Johansson, K. Cedergren, T. Bauch, and F. Lombardi. Properties of inductance and magnetic penetration depth in (103)-oriented $yba_2cu_3o_{7-\delta}$ thin films. *Phys. Rev. B*, 79(21):214513, Jun 2009.

[50] Yuri Zuev, Mun Seog Kim, and Thomas R. Lemberger. Correlation between superfluid density and tc of underdoped $yba2cu3o6 + x$ near the superconductor-insulator transition. *Phys. Rev. Lett.*, 95(13):137002, Sep 2005.

[51] O.G. Vendik, I.B. Vendik, and D.I. Kaparkov. Empirical model of the microwave properties of high-temperature superconductors. *Microwave Theory and Techniques, IEEE Transactions on*, 46(5):469 –478, may 1998.

[52] Fredrik Persson. *Fast dynamics and measurements of single-charge devices*. PhD thesis, Chalmers University of Technology, 2010.